Editors' Suggestion

Disordered boundaries destroy bulk phase separation in scalar active matter

Ydan Ben Dor,* Sunghan Ro,* and Yariv Kafri
Department of Physics, Technion–Israel Institute of Technology, Haifa 3200003, Israel

Mehran Kardar
Department of Physics, Massachusetts Institute of Technology, Cambridge, Massachusetts 02139, USA

Julien Tailleur
Université de Paris, Laboratoire Matière et Systèmes Complexes (MSC), UMR 7057 CNRS, F-75205 Paris, France

(Received 29 August 2021; revised 6 October 2021; accepted 11 January 2022; published 8 April 2022)

We show that disordered boundaries destroy bulk phase separation in scalar active systems in dimension $d < d_c = 3$. This is in strong contrast with the equilibrium case where boundaries have no impact on the bulk of phase-separated systems. The underlying mechanism is revealed by considering a localized deformation of an otherwise flat wall, from which the case of a disordered boundary can be inferred. We find long-ranged correlations of the density field as well as a cascade of eddies which we show prevent bulk phase separation in low enough dimensions. The results are derived for dilute systems as well as in the presence of interactions, under the sole condition that the density field is the unique hydrodynamic mode. Our theoretical calculations are validated by numerical simulations of microscopic active systems.

DOI: 10.1103/PhysRevE.105.044603

I. INTRODUCTION

Active matter refers to a class of nonequilibrium systems in which individual particles are self-propelled due to an irreversible consumption of energy. Their physics is relevant to systems ranging from biological to manmade materials [1–7]. They have attracted much attention since they exhibit a host of novel collective behaviors which cannot be found in equilibrium systems. Examples range from the transition to collective motion, through low-Reynolds turbulence, to motility-induced phase separation (MIPS) [4,7–26]. The latter corresponds to the ability of active systems to phase separate, even when there are no attractive interactions between the particles.

It has been long realized, experimentally and theoretically [5,27–33], that the *shapes* of boundaries in active systems lead to interesting effects, from the rotation of asymmetric gears [34,35] to the emergence of ratchet currents [5,36]. It is tempting to assume that these effects are localized to the wall, on microscopic scales set by the particles' persistence lengths, the potential shapes, and the correlation lengths set by interactions. Consequently, much of the theoretical work on bulk collective behaviors, in particular for dry scalar active matter, has focused on systems which are either infinite or subject to periodic boundary conditions [3,4,37]. The underlying salient assumption is that, much like in equilibrium, the precise nature of the boundaries only affects a subextensive region in macroscopic active systems and thus does not influence their *bulk* behaviors.

In this article, we show that this is generically not the case, even for dry, scalar active matter where boundaries are expected to have the weakest influence. This is illustrated in Fig. 1, which compares the fate of passive and active phase separation in the presence of a disordered wall. As expected [38], the disordered boundary leaves the phase-separated equilibrium system unaffected [Figs. 1(a)–1(d)]. In striking contrast, the disordered wall washes out phase separation in the active case [Figs. 1(e)–1(h)], thus strongly altering the phase diagram. In fact, we demonstrate that phase separation is destroyed by disordered boundaries in dimension $d < d_c = 3$. As we show below, this is a result of disordered boundaries inducing scale-free density modulations and eddy cascades deep in the bulk of active systems. These can already be seen, upon close inspection, in the dilute limit, as illustrated in Fig. 2, showing that disordered boundaries do not solely lead to the localized effects that had been reported earlier [36,39–41].

To investigate the physics behind the numerical results reported in Figs. 1 and 2, we start, in Sec. II, by considering a dilute system in the presence of a localized deformation on an otherwise flat wall. We show that it induces nonstandard boundary conditions on the density and current fields. Using appropriate Green's functions, we show that the perturbation induces a long-range modulation in the steady-state density profile, which we characterize in the far-field limit. We then show in Sec. III how these results allow us to describe a disordered wall and to evaluate the disorder-averaged two-point correlation functions of the density and current fields. These results, first derived in the dilute limit in Sec. III are then generalized to interacting systems in Sec. IV. Finally, we show in Sec. V that, even though the density modulations and currents decay as power laws in the bulk of the system, they are sufficient to destroy MIPS in dimension $d < d_c = 3$. In practice, the wall creates a disordered combination of

*These authors contributed equally to this work.

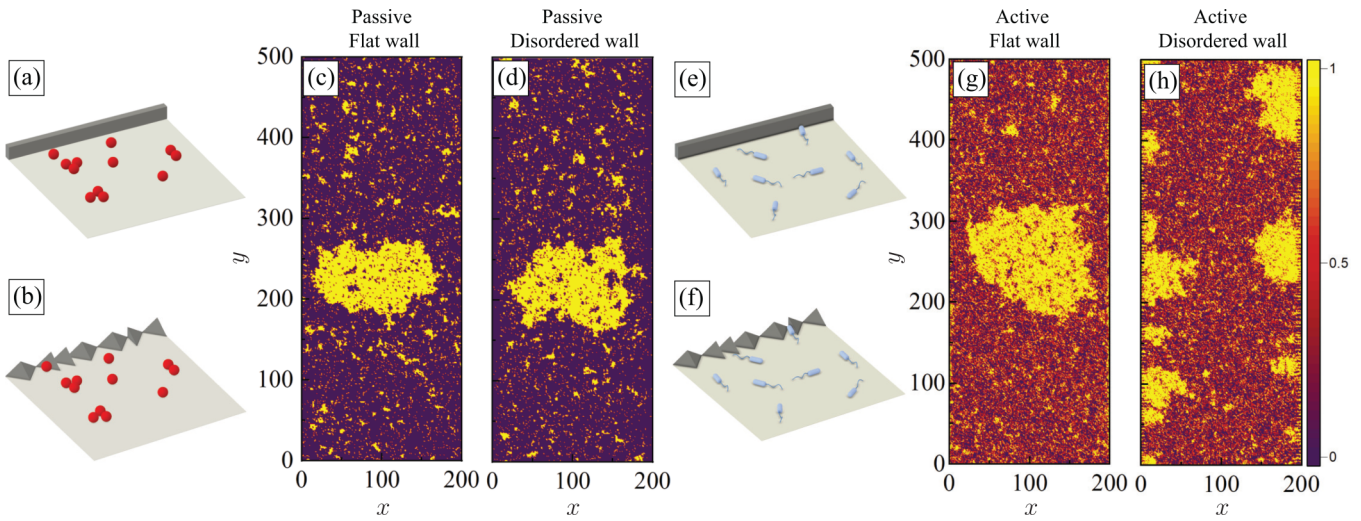

FIG. 1. Impact of flat (a), (e) and disordered walls (b), (f) on phase separation in passive (a), (b) and active (e), (f) systems. In the presence of attractive interactions, simulations of a passive lattice gas at low temperature shows phase separation in both settings (c), (d). In contrast, simulations of an active lattice gas (h) show that the disordered boundary destroys the phase separation observed in the presence of a flat wall (g). Color encodes density; see Appendix A for further numerical details.

long-range attractive and repulsive forces that prevent both bulk phase separation as well as a uniform wetting of the wall by a dense phase.

II. LOCALIZED DEFORMATION ON A FLAT WALL

A. Two dimensions

In this section, we focus on the theoretical models of noninteracting active Brownian particles (ABPs) and run-and-tumble particles (RTPs). For simplicity, our calculations are carried out in two dimensions, and we present the results for higher dimensions in the next subsection. Each active particle follows the Langevin dynamics

$$\frac{d\mathbf{r}_i}{dt} = v\mathbf{u}(\theta_i) - \mu\nabla V(\mathbf{r}_i) + \sqrt{2\mathcal{D}_t}\boldsymbol{\eta}_i(t), \tag{1}$$

$$\frac{d\theta_i}{dt} = \sqrt{2\mathcal{D}_r}\xi_i(t), \tag{2}$$

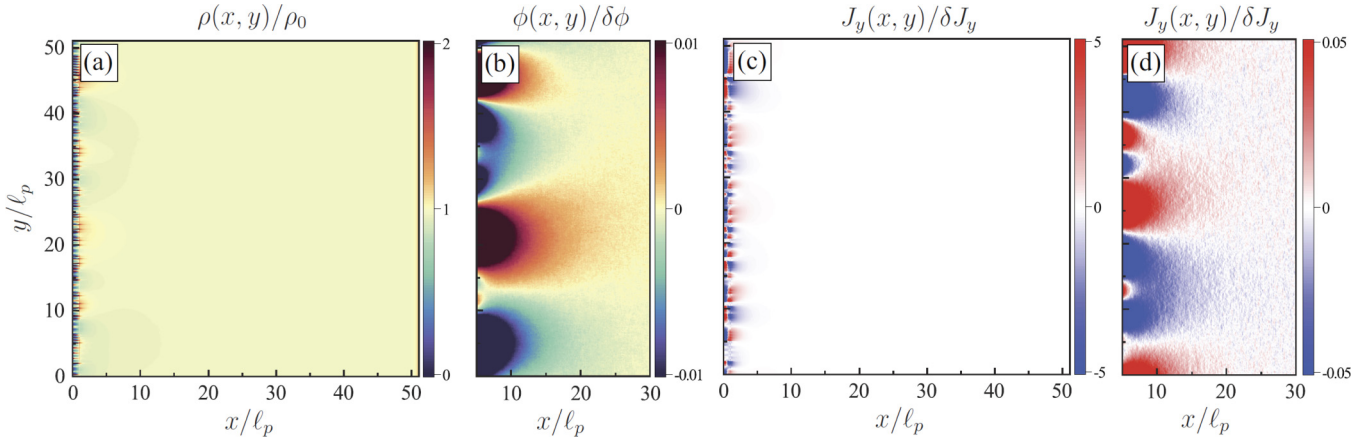

FIG. 2. Steady-state density and currents for run-and-tumble particles on a lattice, in the presence of a disordered wall at $x = 0$ and periodic boundary conditions along the $\hat{\mathbf{y}}$ direction. The disordered wall is modeled as a random potential which vanishes for x larger than the particle persistence length ℓ_p; for other numerical details, see Appendix A. (a) Particle density $\rho(x, y)$ in the full system, normalized by the average density. Lengths are rescaled by the particle run length ℓ_p. Note the presence of a strong density accumulation close to the wall at $x = 0$ that is modulated by the disorder. The color code corresponds to $\rho(x, y)/\rho_0$. (b) Density modulation $\phi(x, y) \equiv \rho(x, y) - \langle\rho(x)\rangle$ in the bulk of the system, where $\langle\rho(x)\rangle$ is the average density at a distance x from the wall, normalized by the standard deviation of the density modulation $\delta\phi$. The density modulations extend deep in the bulk of the system, far beyond the microscopic scales set by the particle run length and the disordered wall. (Note that the x axis starts at five run lengths from the wall.) (c) Current along the $\hat{\mathbf{y}}$ direction in the full system, normalized by the current standard deviation δJ_y. At this scale, a localized current flowing along the wall is observed, as expected from the existing literature [36]. (d) A close-up on the bulk region shown in panel (b) reveals the existence of large eddies whose scales increase with the distance from the wall.

where $\mathbf{r}_i$ is the position of particle i, v its self-propulsion speed, and $\mathbf{u}(\theta_i) = (\cos\theta_i, \sin\theta_i)$ its orientation. The particle mobility is denoted as μ while $\mathcal{D}_t$ and $\mathcal{D}_r$ are the translational and rotational noise amplitudes. Finally, $\boldsymbol{\eta}_i$ and ξ_i are Gaussian white noises of unit variance and zero mean. In addition, the particle heading undergoes complete random reorientations, called tumbles, with rate α. ABPs and RTPs correspond to the limiting cases $\alpha = 0$ and $\mathcal{D}_r = 0$, respectively. The walls are modeled through the external potential $V(\mathbf{r})$. Our theoretical computations are carried out in a semi-infinite domain $x > 0$ in the presence of a flat wall, perpendicular to the $\hat{\mathbf{x}}$ direction, assuming a bulk density ρ_b at $x = +\infty$. An asymmetric obstacle of characteristic size a, representing a localized deformation of the wall, is located at $y = 0$, as illustrated in the inset of Fig. 3(a). The obstacle is modeled as a potential $U(\mathbf{r})$ which is included in $V(\mathbf{r})$.

In this section we show that this deformation induces a steady-state density modulation whose far-field expression is given by

$$\rho(\mathbf{r}) \underset{x\gg a,\ell_p}{\simeq} \rho_b + \frac{\mu}{\pi\mathcal{D}_{\rm eff}}\frac{yp}{r^2} + O(1/r^2). \tag{3}$$

Here $r = \sqrt{x^2+y^2}$ is the distance from the deformation, $\mathcal{D}_{\rm eff} = \mathcal{D}_t + \frac{1}{2}v\ell_p$ is the effective diffusion coefficient, and $\ell_p = v/(\alpha+\mathcal{D}_r)$ is the particle's persistence length. The scale of the modulation is set by p, which measures the net force exerted by the obstacle on the active particles along the wall through

$$p = -\int_0^\infty dx' \int_{-\infty}^\infty dy'\, \rho(\mathbf{r}')\partial'_y U. \tag{4}$$

p is generically nonzero for asymmetric obstacles, when $v \neq 0$. In the following, we refer to $\mathbf{p} \equiv p\hat{\mathbf{y}}$ as the *force monopole* induced by the obstacle. Note that p indirectly depends on all microscopic parameters of the dynamics—and in particular the self-propulsion speed v—through $\rho(\mathbf{r}')$. In particular, when v vanishes, $\rho(\mathbf{r})$ is given by the Boltzmann weight so that $\rho(\mathbf{r}')\partial'_y U \propto \partial'_y e^{-\beta U}$, with a y-independent prefactor. Consequently, p vanishes upon integrating over y' and we recover that there is no long-ranged modulation of the density field in the passive case.[1]

The density modulation is accompanied by a current, which is diffusive in the far field $\mathbf{J} \simeq -\mathcal{D}_{\rm eff}\nabla\rho$, and is given by

$$\mathbf{J}(\mathbf{r}) \underset{x\gg a,\ell_p}{\simeq} \frac{\mu}{\pi}\frac{2xy\hat{\mathbf{x}} + (y^2-x^2)\hat{\mathbf{y}}}{(x^2+y^2)^2}p + O(1/r^3). \tag{5}$$

Equation (5) predicts the flow created by a force monopole on the active fluid: It is the nonequilibrium diffusive counterpart of the Stokeslet flow in fluid dynamics, computed in the vicinity of a hard wall. Our results are verified and illustrated numerically in Fig. 3. We now turn to their derivations, which are extended to homogeneous systems with pairwise interactions in Appendix B.

[1]For an asymmetric obstacle immersed in an active bath, p was computed perturbatively in U and shown to vanish as v^2 when $v \to 0$ [43].

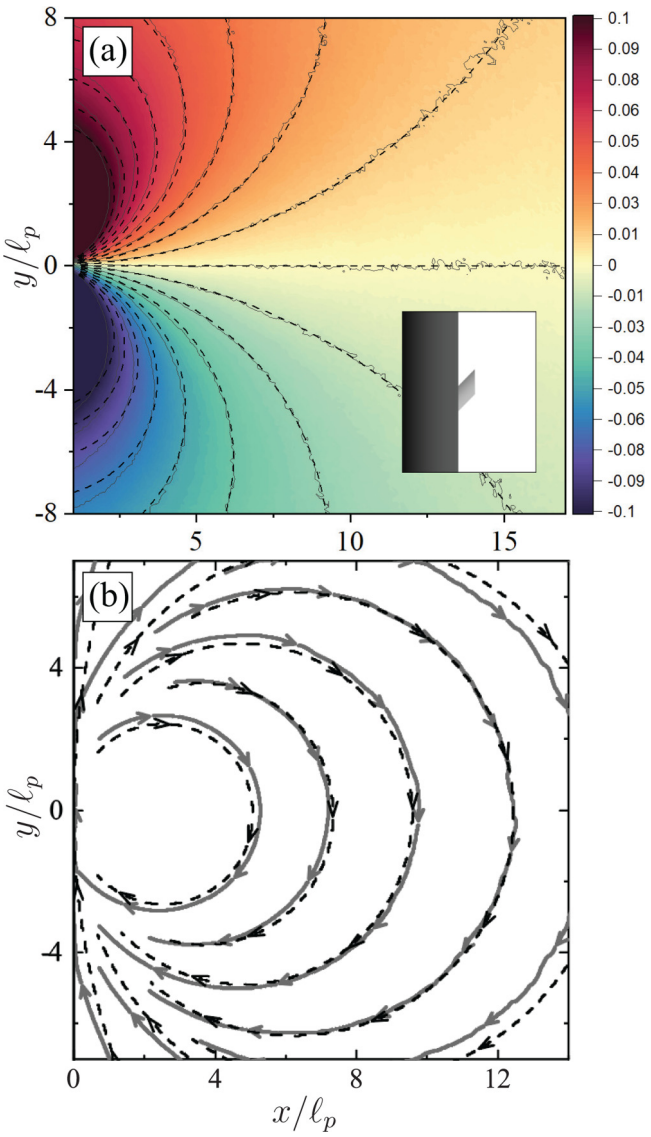

FIG. 3. Density and current of RTPs near a flat wall in the presence of an isolated deformation. (a) The color encodes the density modulation $\phi(x,y) = \rho(x,y) - \langle\rho(x)\rangle$. The solid lines are contour lines plotted every $\delta\phi = 1.25\times10^{-2}$ from the numerical data. They are compared with the corresponding theoretical predictions of Eq. (3), shown by the dashed lines. $\mathbf{p}$ is measured numerically so that there is no fitting parameter. (b) Streamlines of current measured in simulations (gray solid lines), compared to the theoretical prediction (5) (in dashed lines). For simulation details, see Appendix A.

The probability density $\mathcal{P}(\mathbf{r},\theta)$ to find an active particle located at $\mathbf{r}$ and oriented at an angle θ evolves according to the master equation:

$$\partial_t\mathcal{P}(\mathbf{r},\theta) = -\nabla\cdot[v\mathbf{u}\mathcal{P} - \mu\nabla V\mathcal{P} - \mathcal{D}_t\nabla\mathcal{P}] + \mathcal{D}_r\partial_\theta^2\mathcal{P} - \alpha\mathcal{P} + \frac{\alpha}{2\pi}\int d\theta'\,\mathcal{P}(\mathbf{r},\theta'). \tag{6}$$

For noninteracting particles, the average density field simply reads $\rho(\mathbf{r}) = \int d\theta\,\mathcal{P}(\mathbf{r},\theta)$. Integrating over θ leads to a conservation equation:

$$\partial_t\rho(\mathbf{r}) = -\nabla\cdot\mathbf{J}, \tag{7}$$

where the current $\mathbf{J}$ is given by

$$\mathbf{J} = v\mathbf{m} - \mu\rho\nabla V - \mathcal{D}_t\nabla\rho. \tag{8}$$

It is the sum of a diffusive contribution due to translational noise, an advective current due to the external potential, and an active contribution proportional to $\mathbf{m} \equiv \int d\theta\, \mathbf{u}(\theta)\mathcal{P}(\mathbf{r},\theta)$. Far away from the wall and the obstacle, the active dynamics is diffusive at large scales so that we expect $\mathbf{J} \simeq -\mathcal{D}_{\rm eff}\nabla\rho$ in the steady state [15]. We can then introduce

$$\boldsymbol{\mathcal{J}} \equiv \mathbf{J} + \mathcal{D}_{\rm eff}\nabla\rho, \tag{9}$$

which measures the difference between $\mathbf{J}$ and its bulk value to recast the conservation equation in the steady state, $\nabla\cdot\mathbf{J} = 0$, as

$$\mathcal{D}_{\rm eff}\nabla^2\rho = \nabla\cdot\boldsymbol{\mathcal{J}}(\mathbf{r}). \tag{10}$$

Equation (10) has the appealing feature of being a Poisson equation for the density field with a source term $\nabla\cdot\boldsymbol{\mathcal{J}}(\mathbf{r})$, which is expected to be nonvanishing only close to the wall and the deformation. This equation, however, has to be solved self-consistently since $\boldsymbol{\mathcal{J}}$ depends on ρ and $\mathbf{m}$. Furthermore, a second difficulty comes from the nontrivial boundary condition imposed by the wall. Indeed, taking the limit of a hard wall, the component of the current transverse to the wall has to vanish, so that

$$J_x(0,y) = (-\mathcal{D}_{\rm eff}\partial_x\rho + \mathcal{J}_x)|_{x=0} = 0, \tag{11}$$

where $\mathcal{J}_x$ is the x-component of $\boldsymbol{\mathcal{J}}$. This is neither a Dirichlet nor a Neumann boundary condition on ρ, since $\boldsymbol{\mathcal{J}}$ is nonzero at the wall and depends on the density field. Nevertheless, since ρ by itself is not prescribed on the boundary, we can still use the Neumann-Green's function of the Laplacian,

$$G_N(\mathbf{r}_1,\mathbf{r}_2) = -\frac{1}{2\pi}[\ln(|\mathbf{r}_1-\mathbf{r}_2|) + \ln(|\mathbf{r}_1^\perp-\mathbf{r}_2|)], \tag{12}$$

to solve this boundary value problem. Here $\mathbf{r}^\perp \equiv (-x,y)$ is the image of $\mathbf{r}$ with respect to the wall. Using Green's second identity, one finds [42]

$$\rho(\mathbf{r}) = -\frac{1}{\mathcal{D}_{\rm eff}}\int_0^\infty dx'\int_{-\infty}^\infty dy'\, G_N(x,y;x',y')\nabla'\cdot\boldsymbol{\mathcal{J}}' - \int_{-\infty}^\infty dy'\, G_N(x,y;0,y')\partial_x'\rho'\Big|_{x'=0} + \rho_b, \tag{13}$$

where $\partial_i' = \frac{\partial}{\partial r_i'}$ and $g' = g(\mathbf{r}')$ for any function $g(\mathbf{r})$. Note that there are two important differences between the solution (13) and the density modulation that would be observed around an isolated obstacle in the bulk of an active fluid [43]. First, the Green's functions differ between these two cases. Second, the surface integral in the second line of Eq. (13) would be absent in a bulk problem. Here it ensures that no current flows through the wall.

Let us now analyze the behavior of Eq. (13) in the far field, i.e., when $|x-x'| \gg \ell_p, a$. We first split the divergence of $\boldsymbol{\mathcal{J}}'$ as $\nabla'\cdot\boldsymbol{\mathcal{J}}' = \partial_x'\mathcal{J}_x' + \partial_y'\mathcal{J}_y'$ and consider the contribution of $\partial_x'\mathcal{J}_x'$. Since $\boldsymbol{\mathcal{J}}'$ is, to leading order, nonzero only close to the wall, the Green's function $G_N(x,y;x',y')$ can be expanded in x' around $x' = 0$:

$$G_N(x,y;x',y') \simeq G_N(x,y;0,y') + \frac{x'^2}{2}\frac{\partial^2 G_N(x,y;0,y')}{\partial x'^2},$$

where have used $\partial_x' G_N(x,y;0,y') = 0$ by symmetry. In the far field, $(x')^2(\partial_x')^2 G_N \ll G_N$ so that we neglect the second-order derivative. The integral over x' in Eq. (13) can then be carried out explicitly, and, using Eq. (11), it directly balances with the surface integral, leading to

$$\rho(\mathbf{r}) \underset{x\gg\ell_p,a}{\simeq} \rho_b - \frac{1}{\mathcal{D}_{\rm eff}}\int_0^\infty dx'\int_{-\infty}^\infty dy'\, G_N(x,y;x',y')\partial_y'\mathcal{J}_y'. \tag{14}$$

To evaluate Eq. (14), we multiply Eq. (6) by $\mathbf{u}$ and integrate over θ to show that, in the steady state, $\frac{v}{\mu}\mathbf{m} = \nabla\cdot\sigma^a$, where

$$\sigma_{ij}^a = -\frac{\ell_p}{\mu}\left[\frac{v\delta_{ij}\rho}{2} + vQ_{ij} - (\mu\partial_j V + \mathcal{D}_t\partial_j)m_i\right] \tag{15}$$

is known as the active pressure [44–47] and we have introduced $Q_{ij}(\mathbf{r}) \equiv \int d\theta\,(u_iu_j - \frac{\delta_{ij}}{2})\mathcal{P}(\mathbf{r},\theta)$. From the definition of $\boldsymbol{\mathcal{J}}$, one then has

$$\partial_y'\mathcal{J}_y' = \partial_y'\left[-\mu\rho\partial_y'V + \mu\partial_y'\sigma_{yy}' + \mu\partial_x'\sigma_{xy}' + \frac{v\ell_p}{2}\partial_y'\rho\right]. \tag{16}$$

To estimate the leading order contribution to the integral in Eq. (14), we use Eq. (16) and integrate by parts. The three last terms in Eq. (16) lead to two integrations by parts, hence involving the second-order derivative of G_N. In the far field, they can, again, be neglected in comparison to the leading-order term, which reads

$$\rho(\mathbf{r}) \underset{x\gg\ell_p,a}{\simeq} \rho_b - \frac{\mu}{\mathcal{D}_{\rm eff}}\int_0^\infty dx'\int_{-\infty}^\infty dy'\,\rho'\partial_y'U'\partial_y'G_N(x,y;x',y'). \tag{17}$$

Here we have used that U is the only contribution to the potential that is not invariant by translation along y. Using the expression (12) for G_N leads, to leading order in the far field, to Eq. (3).

Remarkably, while we embarked to solve the rather cumbersome problem posed by Eqs. (9) and (10) with the boundary condition (11), the far-field solution (3) can be obtained by solving a simpler problem:

$$\mathcal{D}_{\rm eff}\nabla^2\rho = \mu\nabla\cdot[\mathbf{p}\delta(\mathbf{r})] \tag{18}$$

with $\mathbf{p}$ the force monopole exerted by the deformation and a standard Neumann boundary condition. Because of this simplification, the problem of nontrivial boundaries can now be solved in higher dimensions and for more complex geometries with ease.

B. Higher dimensions

Using Eq. (18), or repeating the above calculation in higher dimensions, leads to

$$\rho(\mathbf{r}) \sim \rho_b + \frac{2\mu}{\mathcal{D}_{\rm eff}S_d}\frac{\mathbf{r}\cdot\mathbf{p}}{r^d} + O(1/r^d), \tag{19}$$

$$\mathbf{J}(\mathbf{r}) \sim \frac{2\mu}{S_d}\frac{d(\hat{\mathbf{r}}\cdot\mathbf{p})\hat{\mathbf{r}} - \mathbf{p}}{r^d} + O(1/r^{d+1}), \tag{20}$$

where $S_d = (2\pi^{\frac{d}{2}})/\Gamma(\frac{d}{2})$ and $\mathbf{p}$ is the force monopole exerted by the obstacle on the active particles along the wall:

$$\mathbf{p} = -\int d^d\mathbf{r}\, \rho(\mathbf{r})\nabla_\parallel U(\mathbf{r}). \tag{21}$$

Here $\nabla_\parallel = \nabla - \hat{\mathbf{x}}\partial_x$ is the derivative operator acting parallel to the wall. Equations (19) and (20) show that the density modulation and flows induced by a localized deformation of a flat wall are solely controlled by the force monopole $\mathbf{p}$ exerted by the deformation on the active particles *along* the wall, induced by asymmetry of the obstacles.

III. DISORDERED BOUNDARIES IN DILUTE ACTIVE SYSTEMS

We now extend the results from an isolated deformation to the case of a disordered wall. The latter is modeled as a potential $V(x, \mathbf{r}_\parallel)$, where $\mathbf{r}_\parallel$ is a $(d-1)$-dimensional vector parallel to the wall. The potential is infinite for $x < 0$ and is localized inside the interval $[0, x_w]$. In that region, $V(x, \mathbf{r}_\parallel)$ is drawn from a random, bounded distribution with a finite correlation length a. As we now show, the far-field modulation of the density field and the current generated by this disordered boundary are identical to those generated by force monopoles randomly placed along a flat wall and parallel to it. To do so, we first compute analytically the current and density modulations created by such random force monopoles and later compare them with microscopic numerical simulations.

A. Long-range density correlations

Consider a continuous, quenched, Gaussian random variable, $\mathbf{f}(\mathbf{r}_\parallel)$, describing the force-monopole density along the wall, whose disorder average satisfies

$$\begin{aligned} \overline{f_i(\mathbf{r}_\parallel)} &= 0, \\ \overline{f_i(\mathbf{r}_\parallel) f_j(\mathbf{r}_\parallel')} &= 2p^2\delta^\parallel_{ij}\sigma^2\delta^{(d-1)}(\mathbf{r}_\parallel - \mathbf{r}_\parallel'), \end{aligned} \tag{22}$$

with p setting the scale of the force, $\sigma^2 \simeq a^{1-d}$ an inverse area related to the microscopic correlation length of V, $\delta^\parallel_{ij} = 1$ if $i = j \neq x$, and $\delta^\parallel_{ij} = 0$ otherwise. To determine the density modulations, we rely on Eq. (18) and solve

$$\mathcal{D}_{\rm eff}\nabla^2\rho = \mu\nabla\cdot[\mathbf{f}(\mathbf{r}_\parallel)\delta(x)], \tag{23}$$

with a Neumann boundary condition. In the far field, this leads to

$$\rho(x, \mathbf{r}_\parallel) \approx \rho_b + \frac{2\mu}{\mathcal{D}_{\rm eff} S_d}\int d^{d-1}\mathbf{r}_\parallel' \frac{(\mathbf{r}_\parallel - \mathbf{r}_\parallel')\cdot\mathbf{f}(\mathbf{r}_\parallel')}{[x^2 + |\mathbf{r}_\parallel - \mathbf{r}_\parallel'|^2]^{\frac{d}{2}}}. \tag{24}$$

We first note that, on average, $\overline{\rho(\mathbf{r})} \approx \rho_b$ in the far field: a disordered wall thus does not generate a systematic density modulation in the far field. However, a nontrivial structure is revealed by computing the disorder-averaged two-point connected correlation function:

$$\overline{\rho(x, \mathbf{r}_\parallel)\rho(x', \mathbf{r}_\parallel')}_c = \frac{1}{S_d}\left(\frac{2\mu p\sigma}{\mathcal{D}_{\rm eff}}\right)^2 \frac{(x + x')}{[(x + x')^2 + |\Delta\mathbf{r}_\parallel|^2]^{\frac{d}{2}}}, \tag{25}$$

where $\Delta\mathbf{r}_\parallel = \mathbf{r}_\parallel - \mathbf{r}_\parallel'$. This equation predicts large-scale density modulations which decay in amplitude—but increase in range—as one moves away from the wall. To see this, consider the case in which $x = x'$. For $\Delta\mathbf{r}_\parallel = 0$, the two-point function decays as $\overline{\rho(x, \mathbf{r}_\parallel)\rho(x, \mathbf{r}_\parallel)}_c \sim 1/x^{d-1}$, showing that the disorder-induced density fluctuations are stronger close to the wall. The transverse correlations of these fluctuations, however, decay only when $|\Delta\mathbf{r}_\parallel| \gg 2x$: their correlation length thus *increases* with the distance from the wall.

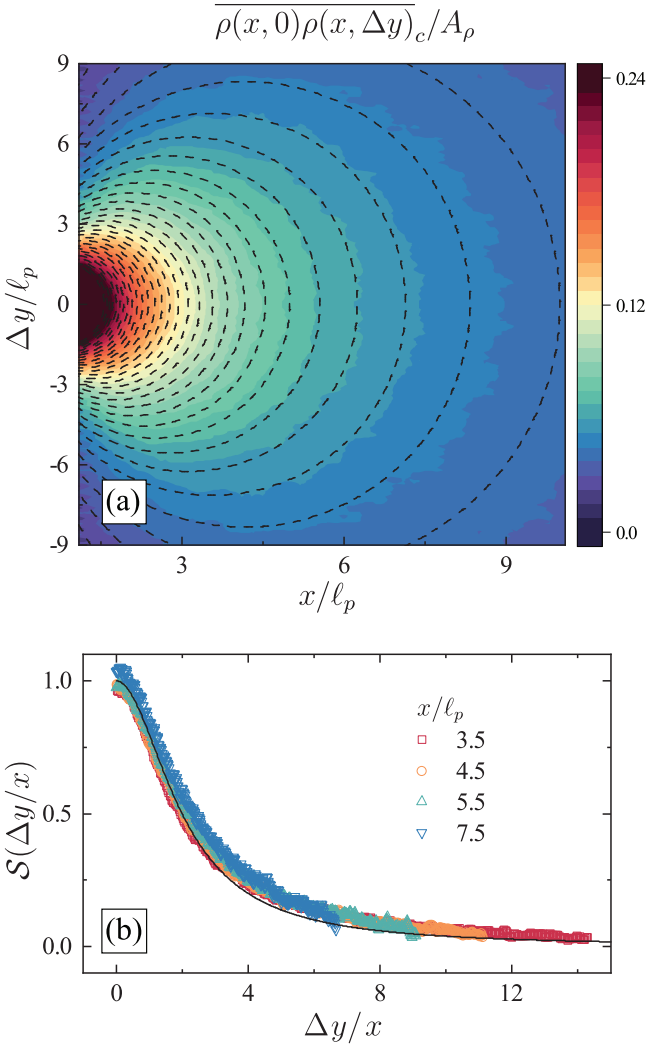

FIG. 4. Disorder-averaged two-point density correlation function of noninteracting RTPs in two dimensions in the presence of a disordered wall at $x = 0$. (a) The two-point correlation function as x and Δy are varied, calculated from simulations, is shown by the color map. The value of $A_\rho \equiv \ell_p S_d^{-1}(2\mu p\sigma/\mathcal{D}_{\rm eff})^2$ is obtained from a fit of the data to Eq. (25). The latter includes a constant offset due to finite-size corrections, which is calculated exactly in Appendix C. The theoretical prediction of Eq. (25) is then used to produce dashed contour lines that match the levels of the color bar. Both theory and simulations are normalized by A_ρ. (b) A verification of the scaling form (26) for the density-density correlation function. The data shown in panel (a) for four different distances x from the wall are collapsed onto a single curve, as predicted. See Appendix A for numerical details.

These results are qualitatively illustrated and quantitatively checked in Fig. 4 using microscopic simulations which demonstrate the relevance of the model (22) for disordered

boundaries. First, we measure numerically $\overline{\rho(x,\mathbf{r}_\parallel)\rho(x,\mathbf{r}_\parallel')}_c$ which we fit against the right-hand side of Eq. (25) to extract the value of σ. The numerical data, normalized by the prefactor $4\mu^2p^2\sigma^2/(S_dD_{\rm eff})$, are then shown to match the contour lines predicted by Eq. (25). A more quantitative comparison can be obtained by noticing that the correlation function can be rescaled as

$$\frac{\overline{\rho(x,y)\rho(x,y+\Delta y)}_c}{\overline{\rho(x,y)\rho(x,y)}_c}=\frac{1}{1+\left(\frac{\Delta y}{2x}\right)^2}\equiv\mathcal{S}\left(\frac{\Delta y}{x}\right),\tag{26}$$

leading to a scaling form. Figure 4(b) shows the quantitative agreement between the numerical data and the prediction of Eq. (26).

B. Current cascade

Another interesting way to interpret these results is to consider the impact of the disordered boundary on the particle current. On a microscopic scale close to the wall, the random forcing induced by the disorder stirs the active medium. The conservation law for the density field then turns this microscopic stirring into large-scale eddies in the bulk of the system. This cascade structure can be quantified by analyzing the statistics of the steady-state currents. In the bulk of the system, the large-scale current can be estimated as [15]

$$\mathbf{J}(x,\mathbf{r}_\parallel)\approx-\mathcal{D}_{\rm eff}\nabla\rho(x,\mathbf{r}_\parallel).\tag{27}$$

Using Eqs. (24) and (27), and performing a Fourier transform with respect to $\mathbf{r}_\parallel$, leads to

$$J_x(x,\mathbf{q}_\parallel)=-i\mu\mathbf{q}_\parallel\cdot\mathbf{f}_{\mathbf{q}_\parallel}\,e^{-|\mathbf{q}_\parallel|x},\tag{28}$$

$$J_k(x,\mathbf{q}_\parallel)=\mathrm{sgn}(q_{\parallel,k})\mu\mathbf{q}_\parallel\cdot\mathbf{f}_{\mathbf{q}_\parallel}\,e^{-|\mathbf{q}_\parallel|x},\tag{29}$$

where k describes one of the $d-1$ dimensions parallel to the wall and $\mathbf{f}_{\mathbf{q}_\parallel}\equiv\int d^{d-1}\mathbf{r}_\parallel\,\mathbf{f}(\mathbf{r}_\parallel)e^{-i\mathbf{q}_\parallel\cdot\mathbf{r}_\parallel}$. Taking a disorder average and using Eq. (22) then leads to

$$\overline{\mathbf{J}(x,\mathbf{q}_\parallel)\cdot\mathbf{J}^*(x,\mathbf{q}_\parallel')}=2d(\mu\sigma p)^2|\mathbf{q}_\parallel|^2e^{-2|\mathbf{q}_\parallel|x}\times(2\pi)^{d-1}\delta^{(d-1)}(\mathbf{q}_\parallel+\mathbf{q}_\parallel').\tag{30}$$

This result shows that, for a given value of x, the current-current correlations first increase for small $|\mathbf{q}_\parallel|$ before they are exponentially suppressed by the term $\exp(-2|\mathbf{q}_\parallel|x)$. The larger the value of x, the smaller the values of $|\mathbf{q}_\parallel|$ for which the peak of the correlation function is observed, revealing eddies on larger and larger scales as x increases. This explains the large-scale structures exhibited by the current in Fig 2. Our predictions (30) are verified quantitatively in Fig. 5, using a scaling form similar to that of Eq. (26).

C. Other geometries

The methodology presented above can be extended to other boundary shapes. For instance, a corrugated border that repeats periodically along the $\hat{\mathbf{y}}$ direction is studied in Appendix C. Our analytical results show the large-scale density-density correlations to be exponentially suppressed at a distance corresponding to the periodicity of the potential. This explains why localized currents had been reported in the presence of periodic asymmetric walls [36], instead of the cascade structure revealed in the previous section.

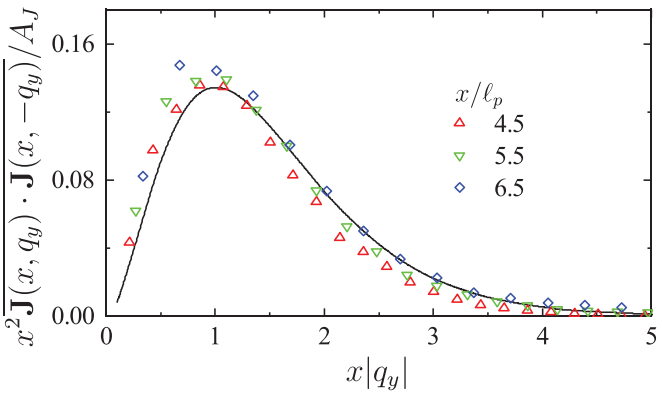

FIG. 5. Fourier transform along the $\hat{\mathbf{y}}$ direction of the current-current correlation function measured at a distance x from the wall and averaged over disorder. The data are measured for three values of x and normalized by a factor $A_J\equiv 2d(2\pi)^{d-1}(\mu\sigma p)^2$. As predicted by our theory, the data can be collapsed onto a single curve, corresponding to Eq. (30), by properly scaling the abscissa and the ordinates. See Appendix A for numerical details.

Another important case pertains to multiple interfering boundaries. For example, Fig. 6 shows the disorder-averaged correlation functions at $x'=x$ for noninteracting RTPs between two disordered walls, with a periodic boundary condition in the $\hat{\mathbf{y}}$ direction. The analytic expression for the correlation function is calculated and given in Appendix D.

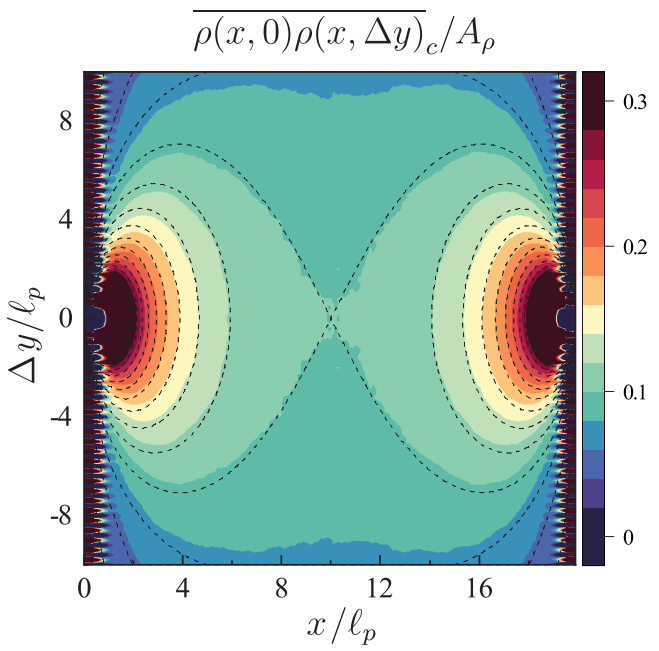

FIG. 6. Disorder-averaged two-point density correlation function of noninteracting RTPs measured in the presence of two disordered walls at $x=0$ and $x=20\ell_p$. Periodic boundary conditions are imposed along the $\hat{\mathbf{y}}$ direction. The correlation function is normalized by a factor $A_\rho\equiv\ell_pS_d^{-1}(2\mu p\sigma/\mathcal{D}_{\rm eff})^2$. Simulation results are shown as a color map and compared to the analytic predictions of Eq. (D2) (dashed contour lines). See Appendix A for numerical details.

In the bulk of the system, the interplay between the two walls leads to a decrease of the transverse correlations and to their suppression in the vicinity of $x = L_x/2$. This highlights how boundaries can control the bulk behaviours of active systems as well as the importance of properly including them in the theoretical description of active matter.

IV. DISORDERED BOUNDARIES IN INTERACTING ACTIVE SYSTEMS

To study the influence of disordered boundaries on interacting active-matter systems, we rely on a linear field theory that builds on the force-monopole picture presented above. Our results are then validated using a self-consistency argument and by the explicit comparison with microscopic numerical simulations.

A. Linear field theory

To proceed, we consider a system of active particles at an average density ρ_b in d space dimensions and consider the density-fluctuation field $\phi(\mathbf{r}) \equiv \rho(\mathbf{r}) - \rho_b$. The particles are in contact with a $d-1$ dimensional wall with a random potential along it. Since the number of particles is conserved, $\phi(\mathbf{r})$ undergoes model B-type dynamics:

$$\partial_t \phi(\mathbf{r}, t) = -\nabla \cdot \mathbf{J}(\mathbf{r}, t), \tag{31}$$

$$\mathbf{J}(\mathbf{r}, t) = -\nabla g[\phi] + \mathbf{f}(\mathbf{r}) + \sqrt{2D}\boldsymbol{\eta}(\mathbf{r}, t). \tag{32}$$

Here $\mathbf{J}(\mathbf{r}, t)$ is a current and $g[\phi]$ plays the role of a chemical potential. We first consider a linear theory in which

$$g[\phi(\mathbf{r}, t)] = u\phi(\mathbf{r}, t) - K\nabla^2\phi(\mathbf{r}, t). \tag{33}$$

$\boldsymbol{\eta}(\mathbf{r}, t)$ is a unit Gaussian white-noise field satisfying

$$\langle \eta_i(\mathbf{r}, t)\eta_j(\mathbf{r}', t')\rangle = \delta_{ij}\delta^d(\mathbf{r} - \mathbf{r}')\delta(t - t'), \tag{34}$$

the mobility has been set to be one, and $K > 0$ for stability. As argued in the previous section, on a coarse-grained scale, the quenched random potential of the boundary amounts to a random force field *along* the wall. We account for it through a quenched random force-density field $\mathbf{f}(\mathbf{r})$ that is parallel to the wall and satisfies

$$f_x(x, \mathbf{r}_\parallel) = 0, \tag{35}$$

$$\begin{aligned} \overline{f_i(x, \mathbf{r}_\parallel)} &= 0, \\ \overline{f_i(x, \mathbf{r}_\parallel) f_j(x', \mathbf{r}'_\parallel)} &= 2s^2\delta_{ij}\delta(x)\delta(x')\delta^{(d-1)}(\mathbf{r}_\parallel - \mathbf{r}'_\parallel), \end{aligned} \tag{36}$$

where i and j label directions parallel to the wall. Note that, in contrast to Eq. (22), we have included the factor $\delta(x)$ in the definition of $\mathbf{f}(\mathbf{r})$. Finally, the strength s of the random force is allowed to depend on ρ_b but is, to leading order, independent of ϕ.

As detailed in Appendix E, the structure factor $S(\mathbf{q}, \mathbf{q}') \equiv \overline{\langle\phi(\mathbf{q})\phi(\mathbf{q}')\rangle}$ can be directly evaluated, leading to

$$\begin{aligned} S(\mathbf{q}, \mathbf{q}') = &\frac{2s^2(2\pi)^{d-1}|\mathbf{q}_\parallel|^2\delta^{(d-1)}(\mathbf{q}_\parallel + \mathbf{q}'_\parallel)}{q^2q'^2(u + Kq^2)(u + Kq'^2)} \\ &+ \frac{2D(2\pi)^{d-1}\delta^d(\mathbf{q} + \mathbf{q}')}{(u + Kq^2)^2}, \end{aligned} \tag{37}$$

where the brackets denote a steady-state average. Interestingly, the long-wavelength behavior is controlled by the random forcing term so that the small q behavior is given by

$$S(\mathbf{q}, \mathbf{q}') \sim (2\pi)^{d-1}\frac{2s^2|\mathbf{q}_\parallel|^2}{u^2(qq')^2}\delta^d(\mathbf{q}_\parallel + \mathbf{q}'_\parallel). \tag{38}$$

In particular, in the limit $q^2, q'^2 \ll u/K$, the correlation function $\overline{\langle\phi(\mathbf{r})\phi(\mathbf{r}')\rangle}$—obtained by performing an inverse Fourier transform on Eq. (37)—agrees with Eq. (25). This allows us to identify $s/u = 2\mu p\sigma/\mathcal{D}_{\text{eff}}$ as the strength of the random forcing in the dilute regime.

B. Self-consistency of the linear field theory

We now check the self-consistency of our linear theory against the addition of nonlinear terms in $g[\phi]$. To do this, we consider

$$g[\phi(\mathbf{r}, t)] = u\phi(\mathbf{r}, t) - K\nabla^2\phi(\mathbf{r}, t) + g\phi^n(\mathbf{r}, t), \tag{39}$$

with $n \geqslant 2$, and examine the scaling of the coefficient of g under the rescaling

$$\mathbf{r} \to b\mathbf{r}, \quad t \to b^z t, \quad \phi \to b^\chi \phi. \tag{40}$$

The dynamic exponent $z = 2$ is diffusive.[2] At the fixed point of the linear theory, Eq. (38) has to be preserved under rescaling. The coupling (s^2/u^2) in Eq. (38) renormalizes as

$$\left(\frac{s^2}{u^2}\right)' = b^{-2\chi-d+1}\left(\frac{s^2}{u^2}\right), \tag{41}$$

which sets

$$\chi = \frac{1-d}{2}. \tag{42}$$

The nonlinearity is thus rescaled as $g \to b^{(n-1)(1-d)/2}g$. For $d > 1$, the term $g\phi^n$ is irrelevant. Note that, consistent with the result of the previous subsection, the term $K\nabla^2\phi$ is also irrelevant, as would any higher-order gradient terms like $(\nabla\phi)^2$. All in all, the linear theory is thus self-consistent for $d > 1$. We now turn to the numerical verification of Eq. (38) using microscopic simulations of interacting active particles.

C. Numerical results

We performed numerical simulations of the microscopic active lattice gas described in Appendix A in the presence of partial exclusion. The scaling form of the correlation function (26) is verified numerically in Fig. 7. The boundary-induced long-ranged correlations revealed in dilute active systems are thus robust to the addition of interactions, hence validating our linear field theory.

The latter describes active systems as long as the density field remains the sole hydrodynamic field. As such, the large-noise disordered phases encountered in the presence of aligning interactions, whether polar or nematic, will exhibit a similar behavior. In particular, this means that the bulk

[2]This can be confirmed, for instance, using the two-point two-time correlation function of the density field. In the large b limit, it admits a nontrivial scaling form only if $z = 2$.

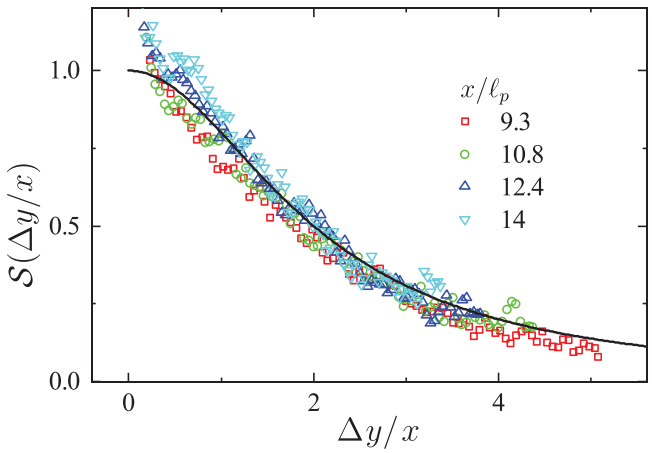

FIG. 7. Scaled density-density correlation function defined in Eq. (26) for interacting RTPs. The simulation results, shown in symbols, are obtained by varying Δy at fixed x. The solid line corresponds to the theoretical prediction of Eq. (26). See Appendix A for numerical details.

large-scale behavior of scalar active matter in the presence of disordered boundaries is controlled by the boundary and *not* by particle interactions.

Our results suggest that the studies of bulk phase transitions of scalar active systems are likely to yield different results depending on the type of boundaries. Unlike in equilibrium systems, the generalization of results obtained in the presence of periodic boundaries should thus be questioned. To this end, in the next section we study the fate of motility-induced phase separation in the presence of disordered walls.

V. THE EFFECT OF DISORDERED BOUNDARIES ON MIPS

In equilibrium, it is known that liquid-gas phase separation is completely unaffected by the presence of disorder on the boundaries of the system [38]. Their contribution to the free energy is indeed subextensive so that it has no influence on the system's bulk behavior. In this section we show that, for scalar active systems, the situation is dramatically different: the long-ranged density modulations induced by the disordered boundaries lead to the suppression of bulk phase separation in any dimensions $d < d_c$ with $d_c = 3$.

To show this, we rely on our linear field theory, Eqs. (31)–(33) and use a Helmholtz-Hodge decomposition of the random forcing:

$$\mathbf{f}(\mathbf{r}) = -\nabla U(\mathbf{r}) + \mathbf{j}(\mathbf{r}). \tag{43}$$

We identify $U(\mathbf{r})$ as an effective potential while $\mathbf{j}(\mathbf{r})$ captures the divergence-free part of the force field. The dynamics of Eq. (31) then implies that the statistics of the density field are insensitive to $\mathbf{j}(\mathbf{r})$. Scalar active systems with disordered boundaries thus share the bulk behavior of a passive equilibrium problem with an effective potential $U(\mathbf{r})$ that we now characterize.

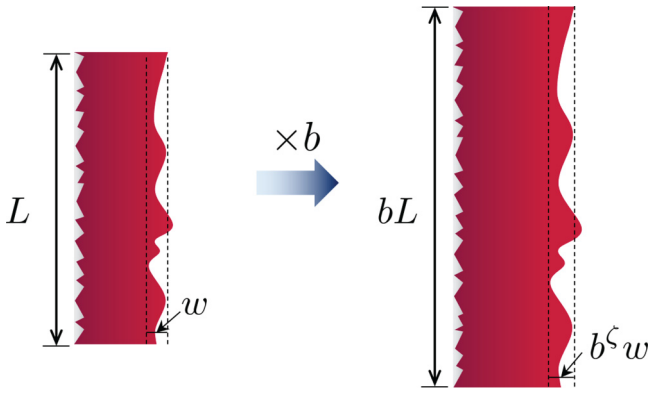

FIG. 8. An illustration of the scaling procedure used to construct the Imry-Ma argument. As the system size is increased by a factor of b, the width of the interface between the phases is multiplied by b^ζ. The interface is well defined in the large system-size limit when $\zeta < 1$.

By definition, the effective potential satisfies $\nabla^2 U(\mathbf{r}) = -\nabla \cdot \mathbf{f}(\mathbf{r})$. Using Eq. (35), it is then straightforward to show that the effective potential obeys

$$\overline{U(\mathbf{r})} = 0, \tag{44}$$

$$\overline{U(\mathbf{r})U(\mathbf{r}')} = \frac{s^2}{S_d} \frac{(x + x')}{[(x + x')^2 + |\Delta \mathbf{r}_\parallel|^2]^{d/2}}. \tag{45}$$

With this in mind, we construct an Imry-Ma argument [48–50] to determine when a phase-separated profile is stable against boundary disorder (see Fig. 8). It is well known that active particles tend to wet hard boundaries so that the liquid phase is usually localized in their vicinity [see Fig. 9(a)]. We thus study the fate of a macroscopic, fully wetting layer of the liquid phase when increasing the system size. Alternatively, we discuss the case of a macroscopic liquid droplet in the bulk of the system in Appendix F, which leads to identical conclusions.

To examine the stability of the wetting configurations, we study the roughness of the interface separating the dense and dilute phases [51]. Its location is described by a height function $h(\mathbf{r}_\parallel)$, with $\mathbf{r}_\parallel$ being the coordinate along the wall. Upon rescaling the system size $\mathbf{r} \to b\mathbf{r}$, the interface width scales as $w \to b^\zeta w$. For a phase-separated configuration to be macroscopically stable, the roughness exponent must satisfy $\zeta < 1$. Otherwise, the existence of a well-defined interface is not self-consistent.

To compute ζ, we consider an interface fluctuating around a mean height h_0. The elastic contribution of the interface to the free energy is given by

$$E_\gamma = \int_{L^{d-1}} d^{d-1}\mathbf{r}_\parallel \left[\frac{\gamma}{2}(\nabla h(\mathbf{r}_\parallel))^2\right], \tag{46}$$

while the change due to the effective potential reads

$$E_U = \int_{L^{d-1}} d^{d-1}\mathbf{r}_\parallel \int_0^{\delta h(\mathbf{r}_\parallel)} dh' \, [\rho_0 U(\mathbf{r}_\parallel, h_0 + h')], \tag{47}$$

where γ is the stiffness of the interface and $\delta h(\mathbf{r}_\parallel) \equiv h(\mathbf{r}_\parallel) - h_0$. To proceed, we compare the scalings of E_γ and E_U upon

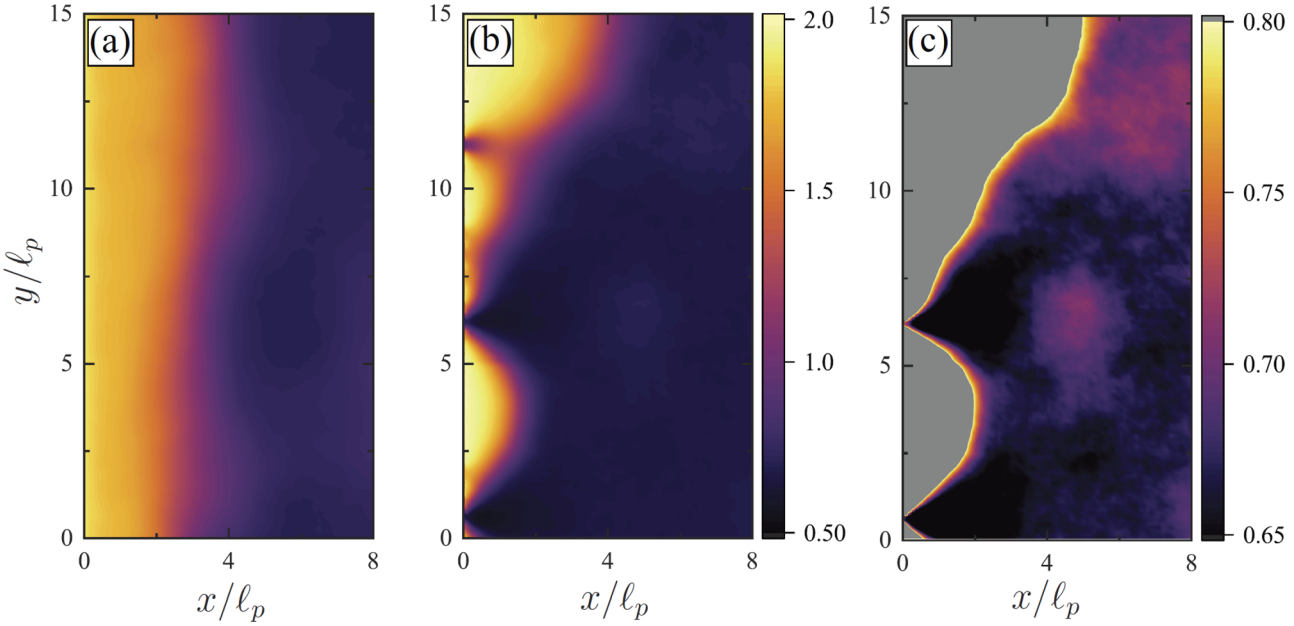

FIG. 9. Time-averaged density of interacting RTPs. (a) Density field in the presence of a hard flat wall at $x = 0$, in the absence of disorder. (b) The density field in the presence of disorder along the wall. The uniform wetting layer shown in panel (a) is broken into random patches of varying size that prevent macroscopic phase separation. (c) The same as (b) with a smaller density range that reveals the long-ranged density modulations in the bulk of the system.

multiplying the system size by a factor of b. By definition, the latter implies $h_0 \to bh_0$ and $\delta h \to b^\zeta \delta h$. Inspection of Eq. (46) shows that E_γ is rescaled as $E_\gamma \to b^{2\zeta+d-3}E_\gamma$. The scale of E_U can be estimated from $|E_U| \equiv \sqrt{\overline{E_U^2}}$, which leads to $E_U \to b^{(d-1+2\zeta)/2}E_U$.

In a phase-separated system, where the interface is well defined, its fluctuations are set by the balance between E_γ and E_U. This requires matching their scaling exponents, which leads to

$$\zeta = \frac{5-d}{2}. \tag{48}$$

Importantly, phase separation with a smooth interface requires $\zeta < 1$, which is only possible for $d > 3$. For dimensions $d < d_c$ with $d_c = 3$, the width of the interface would diverge faster than the size h_0 of the domain: Phase separation is no longer possible. MIPS is thus unstable against boundary disorder for dimensions $d < d_c$ with $d_c = 3$.

Our predictions above are demonstrated numerically in Fig. 9 using interacting RTPs on lattice in $d = 2$. In Figs. 9(a) and 9(b), we compare the steady-state densities of RTPs with and without disorder along the wall. (See Appendix A for details.) In the absence of disorder, a stable phase separation is observed in the form a macroscopic, fully wetting layer. In contrast, in the presence of disorder along the wall, a broken interface is observed, consistent with our Imry-Ma argument. Closer inspection of the bulk, shown in Fig. 9(c), reveals large-scale correlations reminiscent of the noninteracting case. Indeed, as predicted, the density field in the bulk exhibits long-ranged correlations consistent with Eqs. (25) and (38). This is shown in Fig. 7.

Finally, to illustrate dynamically how wall disorder suppresses phase separation in the bulk of the system, we report in Supplemental Material (SM) Movie 1 [52] the following numerical experiment. A system is simulated in the presence of flat walls in the absence of wall disorder, leading to a macroscopic phase separation. To complement the above discussion, we choose parameters such that the macroscopic liquid droplet is deep in the bulk of the system. Then the flat walls are replaced by disordered ones and the system is let to relax. The bulk droplet evaporates and is randomly redistributed across the system, consistent with the Imry-Ma argument of Appendix F.

VI. CONCLUSIONS

In this work, we have shown that disordered boundaries exert a surprising influence on the bulk of active systems, leading to long-ranged correlations, current cascades, and the destruction of bulk phase separation. Our results are valid for scalar active matter and are robust to interactions between the particles as long as density remains the sole hydrodynamic field. This strongly differs from equilibrium systems in which the influence of boundaries can generically be discarded (for an interesting exception, see [53]). Our results were derived for RTPs and ABPs, but they can be straightforwardly extended to other classes of active particles like active Ornstein-Uhlenbeck particles [54,55].

Experimentally, the sensitivity of active matter to boundaries has attracted significant attention in the past [27,56]. In response, many boundary designs have been suggested to suppress their impact on the system [28]. Our work shows that boundary effects are not restricted to finite-size systems and would persist in the thermodynamic limit. By offering a quantitative way to account for the influence of boundaries, we instead raise the question as to how boundaries can be used to control the bulk properties of active systems. Answering this

challenging question will require adapting the methodology developed in this article to more general boundary shapes.

ACKNOWLEDGMENTS

We thank Ari Turner for useful discussions. Y.B.D., S.R., Y.K., and M.K. were supported by NSF5-BSF Grant No. DMR-170828008. Y.B.D., S.R., and Y.K. acknowledge support from an ISF grant. J.T. acknowledges support from ANR grant THEMA. All authors benefited from participation in the 2020 KITP program on Active Matter supported by Grant No. NSF PHY-1748958.

APPENDIX A: NUMERICAL SIMULATIONS

All our numerics on active systems correspond to RTPs in two dimensions. Our theoretical predictions were successfully tested against both off-lattice and on-lattice simulations. In this article, we solely report the latter for which larger sizes and times can be reached.

We consider N RTPs with and without interactions on a two-dimensional lattice of size $L_x \times L_y$. The system is periodic along the $\hat{\mathbf{y}}$ direction and confined by hard walls at $x < 0$ and $x \geqslant L_x$.

1. Disordered wall

The quenched disordered potential is modeled by placing wedge-shaped asymmetric obstacles along the wall, at every $\delta y = \ell_w$, whose orientations are chosen randomly (see Fig 1 for a qualitative illustration). The obstacles have a finite extent x_w in the $\hat{\mathbf{x}}$ direction.

To be more precise, we define $V_{\mathbf{i}} \equiv V_{x,y}$ the potential felt by the particles at site $\mathbf{i} \equiv (x, y)$. The kth wedge-shaped obstacles is thus defined by a potential in $[0, x_w] \times [(k-1)\ell_w, k\ell_w]$:

$$V^{\epsilon,k}_{x,y} = \frac{A^{\epsilon}_{y-(k-1)\ell_w}}{x_w}(x_w - x)\Theta(x_w - x), \tag{A1}$$

which is a locally linear function of x with an amplitude $A^{\epsilon}_{y-(k-1)\ell_w}$ that is a linear function of y. Here $\Theta(x)$ is a Heaviside step function and $\epsilon = \pm 1$ is chosen at random for each value of k with equal probability, to decide the obstacles orientations. The y-dependent amplitudes $A^{\pm}_{y-(k-1)\ell_w}$ of the kth obstacle is then given by

$$A^{+}_{y} = \frac{\Delta V}{\ell_w} y\Theta(y)\Theta(\ell_w - y), \tag{A2}$$

$$A^{-}_{y} = \frac{\Delta V}{\ell_w}(\ell_w - y)\Theta(y)\Theta(\ell_w - y). \tag{A3}$$

All in all, with these building blocks, the wall disordered potential $V_{x,y}$ is given by

$$V_{x,y} = \sum_{k=1}^{L_y/\ell_w} V^{\epsilon_k,k}_{x,y}, \tag{A4}$$

where L_y is chosen to be an integer multiple of ℓ_w and ϵ_k is the orientation of the kth wedge. If the second wall, at $x = L_x$, is also disordered, as in Fig. 6, its potential is obtained by substituting x with $L_x - 1 - x$ in Eq. (A4) and by sampling independently the orientations along the wall at $x = L_x$. This implies that the orientations of the wedges at $x = 0$ and $x = L_x - 1$ are independent of each other.

2. RTP lattice simulations

To simulate RTPs on a square lattice, each particle is assigned an orientation $\mathbf{u}(\theta) = (\cos\theta, \sin\theta)$ where $\theta \in [0, 2\pi)$ and reorients to a new random orientation with a rate α. In the absence of interactions and a disordered potential, the active propulsion of each particle is implemented through a biased hopping of the particles. In practice, a particle hops from a position $\mathbf{i}$ to any of its $2d$ nearest-neighboring sites $\mathbf{j}$ with a rate given by $W_{\mathbf{i},\mathbf{j}} = \max[v\mathbf{u}(\theta)\cdot\hat{\mathbf{e}}, 0]$. Here v is a propulsion speed and $\hat{\mathbf{e}} = \mathbf{j} - \mathbf{i}$. If $\mathbf{j}$ lies inside a hard wall, $W_{\mathbf{i},\mathbf{j}} = 0$. The presence of a nonzero quenched potential disorder, $V_{\mathbf{i}}$, modifies the hopping rates as $W_{\mathbf{i},\mathbf{j}} = \max[v\mathbf{u}(\theta)\cdot\hat{\mathbf{e}} - (V_{\mathbf{j}} - V_{\mathbf{i}}), 0]$. Finally, in simulations where interactions between particles are included, we take the hoping rates as $W^{\text{int}}_{\mathbf{i},\mathbf{j}} = W_{\mathbf{i},\mathbf{j}}(1 - n_{\mathbf{j}}/n_M)$ where $n_{\mathbf{j}}$ is the number of particles at site $\mathbf{j}$ and n_M is the maximal site occupancy. Such interactions are known to lead to motility-induced phase separation provided that v/α and the density are large enough [10] and that $n_M > 1$ [57].

In what follows, we provide parameters and further details on each figure. We define the average density as $\rho_0 \equiv N/(L_x L_y)$.

Figure 1. Instantaneous snapshots of site occupancies of passive and active particles. The passive particles are simulated with the standard Metropolis Monte Carlo rule, with the Hamiltonian given as

$$\mathcal{H} = -\sum_{\{\mathbf{i},\mathbf{j}\}} J n_{\mathbf{i}} n_{\mathbf{j}} + \sum_{\mathbf{i}} V_{\mathbf{i}} n_{\mathbf{i}}, \tag{A5}$$

where the first summation is performed for $\mathbf{i}$ and $\mathbf{j}$ when they are the nearest neighbors of each other and each site can be occupied by at most one particle. On panel (c), we impose hard wall for $x < 0$ and $L_x \leqslant x$, and on panel (d), we add disorder potential beside hard walls. Panels (g) and (h) present snapshots of active particles. On panel (g), we put hard walls similarly to panel (c), and the tumble rates are increased by a factor of 1.5 along the walls to prevent wall accumulation. On panel (h), we add disordered walls along the hard walls. The parameters used are $L_x = 2 \times 10^2$, $L_y = 5 \times 10^2$, $n_M = 1$ for (c) and (d), $n_M = 2$ for (g) and (h), $\rho_b/n_M = 0.45$, $J = 1.8 k_B T$, $v = 9.5$, $\alpha = 1$, $\Delta V = 6 k_B T$ for (c) and (d), $\Delta V = 22$ for (g) and (h), $x_w = 10$, $\ell_w = 3$, $t_0/\Delta t = 2 \times 10^6$ for (g) and (h), and 8×10^6 Monte Carlo sweeps have been performed before obtaining the snapshots for (c) and (d).

Figure 2. The steady-state density and the current for a single realization of the disordered wall at $x = 0$. On panel (a), the steady-state density $\rho(x, y)$ is defined as the time average of the number of particles $n_{\mathbf{i}}$ at $\mathbf{i} = (x, y)$. On panel (b), we present the density modulation $\phi(x, y) \equiv \rho(x, y) - \langle\rho(x)\rangle$ measured with respect to $\langle\rho(x)\rangle$, defined as the time average of $\rho(x) \equiv L_y^{-1}\sum_{y=0}^{L_y} n_{x,y}$.

On panels (c) and (d), the current along the y-axis $J_y(x, y)$ is measured as follows. We define $h_{y,\mathbf{i}}$, the number of particles that hop from $\mathbf{i} = (x, y)$ to $(x, y+1)$ during a time interval t_0, and then evaluate the current as $J_y(x, y) = (h_{y,\mathbf{i}} + h_{y\mathbf{i}-\mathbf{1}})/(2t_0)$.

The data are normalized using $\delta\phi$ and δJ_y, which are the standard deviations of the density and of J_y computed for each site and averaged over the whole lattice.

The parameters used are $L_x = 2^9$, $L_y = 2^9$, $\rho_0 = 0.2$, $v = 10$, $\alpha = 1$, $\Delta V = 20$, $x_w = 10$, $\ell_w = 4$, and $t_0/\Delta t = 2 \times 10^7$ with $\Delta t = (\alpha + \sqrt{2}v + 2\Delta V)^{-1}$ the unit time of the lattice simulation.

Figure 3. The steady-state density and current streamlines for an isolated localized deformation at $x = 0$. Here the deformation is modeled by the potential

$$V_{x,y} = \frac{\Delta V}{\ell_w}(y - x)\Theta(y - x)\Theta(\ell_w + x - y)\Theta(x_w - x).$$

The streamlines shown in Fig. 3(b) are obtained using the streamline plot module of OriginLab. The parameters used are $L_x = 2.2 \times 10^2$, $L_y = 6.6 \times 10^2$, $\rho_0 = 1.0$, $v = 6$, $\alpha = 1$, $\Delta V = 10$, $x_w = 6$, $\ell_w = 5$, and $t_0/\Delta t = 6 \times 10^7$.

Figure 4. A plot of the steady-state two-point density correlation function $\overline{\phi(x, y)\phi(x, y + \Delta y)}_c$ in the presence of a disordered wall at $x = 0$. The simulation data used to evaluate the correlations are coarse-grained, so that the value of the correlation function at $\mathbf{i}$ is obtained by taking an average over the 5×5 lattice sites centered at $\mathbf{i}$. The data are then fitted to Eq. (C7) to extract the value of $A_\rho \equiv \ell_p S_d^{-1}(2\mu p\sigma/\mathcal{D}_{\rm eff})^2$. We then normalized the data by A_ρ and added the finite-size correction $\pi\ell_p/L_y$ before comparing to the theoretical prediction, consistent with the finite-size results of Appendix C.

The parameters used are $L_x = 3 \times 10^2$, $L_y = 1.5 \times 10^3$, $\rho_b = 0.2$, $v = 10$, $\alpha = 1$, $\Delta V = 20$, $x_w = 10$, $\ell_w = 4$, $t_0/\Delta t = 4 \times 10^6$. The disorder average is taken over 1.3×10^3 independent realizations.

Figure 5. Scaling of the current-current correlation function. To produce this figure, we measure the current two-point correlation function $\overline{\mathbf{J}(x, y) \cdot \mathbf{J}(x, y + \Delta y)}_c$ with the current measured using the procedure described above, but extended to include the current in the $\hat{\mathbf{x}}$ direction. Then a Fourier transform is carried out along the $\hat{\mathbf{y}}$ direction.

The parameters used are $L_x = 2^8$, $L_y = 2^{10}$, $\rho_b = 0.2$, $v = 10$, $\alpha = 1$, $\Delta V = 20$, $x_w = 10$, $\ell_w = 4$, $t_0/\Delta t = 2 \times 10^6$. Disorder averages are taken over 8×10^2 independent realizations.

Figure 6. The density two-point correlation function in the presence of two disordered walls at $x = 0$ and $x = L_x - 1$. Similarly to the figure with a single disordered wall, we coarse grain the data over 5×5 lattice sites. To compare the simulation data and the analytic expression (D2), we use the strength of the random forcing and the finite-size offset as fitting parameters. The theoretical contour lines correspond to the boundaries of the levels of the color bar.

The parameters used are $L_x = 2 \times 10^2$, $L_y = 8 \times 10^2$, $\rho_b = 0.2$, $v = 10$, $\alpha = 1$, $\Delta V = 20$, $x_w = 10$, $\ell_w = 4$, $t_0/\Delta t = 4 \times 10^6$. Disorder averages are taken over 3×10^3 independent realizations.

Figure 7. The current two-point correlation function obtained for interacting RTPs in the presence of a disordered wall at $x = 0$. The steady-state density is measured using the procedure described above. The finite-size offset of the correlation function is used as a fitting parameter. The parameters used are $L_x = 3 \times 10^2$, $L_y = 9 \times 10^2$, $n_M = 2$, $\rho_b = 0.8$, $v = 9.5$, $\alpha = 1$, $\Delta V = 18$, $x_w = 10$, $\ell_w = 3$, and $t_0/\Delta t = 3 \times 10^5$. Note that the tumbling rate is locally enhanced to $\alpha = 3$ when $V_{\mathbf{i}} \neq 0$ to reduce accumulation of the particles along the wall, hence enhancing the signal far away from the wall. The disorder average is taken over 5×10^2 independent realizations.

Figure 9. The steady-state density for interacting RTPs with and without boundary disorder for a single realization of disorder. The parameters used are $L_x = 2 \times 10^2$, $L_y = 6 \times 10^2$, $n_M = 2$, $\rho_b = 0.9$, $v = 9.5$, $\alpha = 1$, $t_0/\Delta t = 10^5$. For panel (a), we set $\Delta V = 0$, and for panels (b) and (c), we set $\Delta V = 18$, $x_w = 10$, $\ell_w = 3$.

SM Movie 1: The system is simulated in the presence of flat walls until MIPS is observed in the form of a single macroscopic liquid droplet coexisting with a gaseous background. To prevent wall accumulation, the tumble rates are increased by a factor of 1.5 along the walls. At $t = 0$, disorder along the wall is turned on and the system is let to relax. The parameters used are $L_x = 2 \times 10^2$, $L_y = 5 \times 10^2$, $n_M = 2$, $\rho_b = 0.9$, $v = 9.5$, $\alpha = 1$, $\Delta V = 22$, $x_w = 10$, $\ell_w = 3$, $t_0/\Delta t = 2 \times 10^6$.

APPENDIX B: MULTIPOLE EXPANSION FOR PAIRWISE-INTERACTING ACTIVE PARTICLES

In this Appendix, we generalize the derivation of the far-field density modulations carried out for noninteracting ABPs and RTPs in Sec. II to allow for pairwise interactions. The derivation is restricted to systems that are homogeneous and, for simplicity, it is carried in two dimensions. The generalization to higher dimensions is straightforward.

We consider active particles evolving according to the dynamics

$$\frac{d\mathbf{r}_i}{dt} = v\mathbf{u}(\theta_i) - \mu\boldsymbol{\nabla}\Big[V(\mathbf{r}_i) + \sum_{j\neq i}\mathrm{u}(|\mathbf{r}_i - \mathbf{r}_j|)\Big] + \sqrt{2\mathcal{D}_t}\boldsymbol{\eta}_i(t), \tag{B1}$$

$$\frac{d\theta_i}{dt} = \sqrt{2\mathcal{D}_r}\xi_i(t). \tag{B2}$$

In addition, the particles' orientations undergo tumbles with rate α. Note that, in comparison to Eqs. (1) and (2), we now allow for interactions between the particles through a pair potential $\mathrm{u}(|\mathbf{r}_i - \mathbf{r}_j|)$.

To proceed, we use Itô calculus [58] to derive an equation for the empirical distribution $\psi(\mathbf{r}, \theta, t) = \sum_i \delta^{(2)}(\mathbf{r}_i - \mathbf{r})\delta(\theta - \theta_i)$. From this it is straightforward [21,59,60] to write a continuity equation for the average density field $\rho(\mathbf{r}, t) = \langle\hat{\rho}(\mathbf{r}, t)\rangle = \langle\sum_i \delta^{(2)}(\mathbf{r} - \mathbf{r}_i)\rangle$,

$$\partial_t\rho = -\boldsymbol{\nabla}\cdot\mathbf{J}. \tag{B3}$$

Here $\mathbf{J}$ is the average particle current and is given by

$$\mathbf{J} = -\mu\rho\boldsymbol{\nabla}V + \mu\ell_p\boldsymbol{\nabla}\cdot[(\boldsymbol{\nabla}V)\mathbf{m}] + \mu\boldsymbol{\nabla}\cdot\boldsymbol{\sigma}, \tag{B4}$$

where the divergence operator is contracted with $\boldsymbol{\nabla}V$ in the second term and $m_\alpha = \langle\hat{m}_\alpha(\mathbf{r}, t)\rangle = \langle\sum_i u_\alpha(\theta_i)\delta^{(2)}(\mathbf{r} - \mathbf{r}_i)\rangle$. $\boldsymbol{\sigma}$ appearing in Eq. (B4) can be interpreted as the stress tensor of the active fluid and is given by

$$\sigma_{ij} = -\frac{\mathcal{D}_{\rm eff}}{\mu}\rho\delta_{ij} + \sigma_{ij}^{\rm P} + \sigma_{ij}^{\rm IK}, \tag{B5}$$

with

$$\boldsymbol{\sigma}^{\mathrm{P}}(\mathbf{r}) = \ell_p \int d^2\mathbf{r}'\, \nabla \mathrm{u}(|\mathbf{r}-\mathbf{r}'|)\langle \hat{\mathbf{m}}(\mathbf{r})\hat{\rho}(\mathbf{r}')\rangle + \frac{\mathcal{D}_t \ell_p}{\mu}\nabla \mathbf{m}(\mathbf{r}) - \frac{v\ell_p}{\mu}\mathbf{Q}(\mathbf{r}), \tag{B6}$$

the contribution to the stress tensor due to the local ordering of the particles' orientations. Here $\mathrm{Q}_{\alpha\beta} = \langle \sum_i [u_\alpha(\theta_i)u_\beta(\theta_i) - \frac{1}{2}\delta_{\alpha\beta}]\delta^{(2)}(\mathbf{r}-\mathbf{r}_i)\rangle$ is the nematic tensor, and

$$\boldsymbol{\sigma}^{\mathrm{IK}}(\mathbf{r}) = \frac{1}{2}\int d^2\mathbf{r}'\, \frac{\mathbf{r}'\mathbf{r}'}{|\mathbf{r}'|}\mathrm{u}'(\mathbf{r}') \times \int_0^1 d\lambda\, \langle \hat{\rho}(\mathbf{r}+(1+\lambda)\mathbf{r}')\hat{\rho}(\mathbf{r}+(1-\lambda)\mathbf{r}')\rangle \tag{B7}$$

is the Irwin-Kirkwood stress tensor. In what follows, we focus on the steady state where $\partial_t \rho = 0$.

Similar to Sec. II, we introduce $\boldsymbol{\mathcal{J}}^\sigma = \mathbf{J} - \mu\nabla\cdot\boldsymbol{\sigma}$, which allows us to recast Eq. (B3) in the steady state, $\nabla\cdot\mathbf{J} = 0$, as

$$\mu\partial_i\partial_j\sigma_{ij} = -\partial_i\mathcal{J}^\sigma_i. \tag{B8}$$

Here summation over repeated indices is implied. Finally, the boundary condition ensuring a vanishing current across the wall can be written as

$$J_x(0,y) = \left(\mu\partial_j\sigma_{xj} + \mathcal{J}^\sigma_x\right)\big|_{x=0} = 0. \tag{B9}$$

In contrast to the derivation of the main text, which deals with a scalar density field, $\boldsymbol{\sigma}$ is here a tensor field, which requires more care. To bring Eq. (B8) to the form of a Poisson equation, we perform a Helmholtz-Hodge decomposition, isolating the divergence-less part of the stress tensor

$$\nabla\cdot\sigma = -\nabla\Phi + \nabla\times\boldsymbol{\Psi}. \tag{B10}$$

Here Φ is a scalar potential and $\boldsymbol{\Psi} \equiv \Psi\hat{z}$ is a vector potential. Taking the divergence of Eq. (B10) along with Eq. (B8), one finds that the field Φ obeys Poisson's equation

$$\mu\nabla^2\Phi = \nabla\cdot\boldsymbol{\mathcal{J}}^\sigma, \tag{B11}$$

with the boundary condition

$$\mu\partial_x\Phi|_{x=0} = (\mathcal{J}^\sigma_x + \mu\partial_y\Psi)|_{x=0}, \tag{B12}$$

similar to the equation satisfied by the density field $\rho(\mathbf{r})$ in the derivation of Sec. II. From this point on, we follow the previous derivation closely. The solution of Eq. (B11) reads

$$\mu\Phi(\mathbf{r}) = -\int_0^\infty dx' \int_{-\infty}^\infty dy'\, G_N(x,y;x',y') \times [\nabla'\cdot\boldsymbol{\mathcal{J}}^{\sigma\prime} + \mu(\nabla'\times\nabla')\cdot\boldsymbol{\Psi}'] - \int_{-\infty}^\infty dy'\, G_N(x,y;0,y')\mu\partial'_x\Phi'\Big|_{x=0} + \mu\Phi_b. \tag{B13}$$

In the expression for $\mu\Phi(\mathbf{r})$, we added $(\nabla'\times\nabla')\cdot\boldsymbol{\Psi}' = (\partial'_x\partial'_y - \partial'_y\partial'_x)\Psi' = 0$ and $\mu\Phi_b$, a constant whose physics we identify later. In the far field $|x-x'| \gg \ell_p, a$, we separate the x' and y' components in the first integral of Eq. (B13) using

$$\nabla\cdot\boldsymbol{\mathcal{J}}^\sigma + \mu(\nabla\times\nabla)\cdot\boldsymbol{\Psi} = \partial_x\left[\mathcal{J}^\sigma_x + \mu\partial_y\Psi\right] + \partial_y\left[\mathcal{J}^\sigma_y - \mu\partial_x\Psi\right],$$

and consider the first contribution. It is nonzero, to leading order, only in the vicinity of the wall and of the obstacle, and we thus Taylor expand the Green's function in the first line of Eq. (B13) in x' near $x' = 0$. As $(x')^2(\partial'_x)^2 G_N \ll G_N$ in the far field, the expansion can be truncated at zeroth order to find

$$\mu\Phi(\mathbf{r}) \underset{x\gg\ell_p,a}{\simeq} \mu\Phi_b - \int_0^\infty dx' \int_{-\infty}^\infty dy'\, G_N(x,y;x',y')\partial'_y[\mathcal{J}^{\sigma\prime}_y - \mu\partial'_x\Psi']. \tag{B14}$$

Using the definition of $\boldsymbol{\mathcal{J}}^\sigma$ along with the expression for the current in Eq. (B4), we find that the term appearing in the integrand of Eq. (B14) is

$$\partial'_y\left[\mathcal{J}^{\sigma\prime}_y - \mu\partial'_x\Psi'\right] = \mu\partial'_y\left\{-\rho\partial'_y U + \ell_p\nabla'\cdot[(\nabla' U)m'_y] - \partial'_x\Psi'\right\}, \tag{B15}$$

where U is the part of the potential that is not invariant under translations along the $\hat{\mathbf{y}}$ direction. We then integrate Eq. (B14) by parts. The leading order contribution in the far field comes solely from the term involving $\rho\partial'_y U$, as it contains less derivatives. With this, the scalar potential $\Phi(\mathbf{r})$ becomes

$$\Phi(\mathbf{r}) \underset{x\gg a,\ell_p}{\simeq} \Phi_b + \frac{1}{\pi}\frac{yp}{r^2} + O(1/r^2), \tag{B16}$$

where $\mathbf{p} = p\hat{\mathbf{y}}$ is given by the same expression as the force monopole obtained in Eq. (4).

To obtain the density profile, we assume that, in the far field, the stress tensor is dominated by local contributions. It is then possible to express $\boldsymbol{\sigma}$ using a gradient expansion

$$\sigma(\mathbf{r}) = \sigma(\rho(\mathbf{r})) + O(\nabla\rho). \tag{B17}$$

Note that the dependence of the solution on Ψ does not enter explicitly into the expression (B16) for Φ; it can be shown that while $\Phi \sim O(1/r)$, the contribution from Ψ is of higher order, namely, $\Psi \sim O(1/r^2)$ (for a detailed discussion, see Ref. [60]). This makes it possible to obtain the pressure directly from Eq. (B16), using $P = -\frac{1}{2}\mathrm{Tr}\,\boldsymbol{\sigma}$,

$$P(\mathbf{r}) = \Phi_b + \frac{1}{\pi}\frac{yp}{r^2} + O(1/r^2), \tag{B18}$$

which allows us to identify $\Phi_b = P_b$ with the bulk pressure of the system [21].

Finally, for the steady-state density profile, we note that, to leading order in the far field, the fluid is barotropic $P(\mathbf{r}) \approx P[\rho(\mathbf{r})]$. Then, neglecting higher orders in the gradient expansion, we expand the pressure near its bulk value

$$P(\mathbf{r}) \underset{x\gg a,\ell_p}{\simeq} P_b + [\rho(\mathbf{r}) - \rho_b]P'(\rho_b) + O((\rho-\rho_b)^2, \nabla\rho), \tag{B19}$$

with ρ_b the bulk density, $[-\rho_b P'(\rho_b)]$ the inverse compressibility, and $P' = \partial P/\partial\rho$. Inverting this relation, we find

$$\rho(\mathbf{r}) \underset{x\gg a,\ell_p}{\simeq} \rho_b + \frac{1}{\pi P'(\rho_b)}\frac{yp}{r^2} + O(1/r^2), \tag{B20}$$

similar to the expression given in Eq. (3) for noninteracting particles.

APPENDIX C: PERIODIC WALLS AND FINITE-SIZE CORRECTIONS

In this Appendix, we first show that periodic and aperiodic walls have very different effects on the surrounding active fluid: While aperiodic walls induce long-range modulations in the bulk of the system, periodic walls only affect a finite-size boundary layer in their vicinity.

To see this in detail, we consider the effect of periodic walls on the steady-state density profile. To do so, we confine the active particles to a semi-infinite cylindrical shell $x > 0$, with y periodic along the $\hat{\mathbf{y}}$ direction, with a period L_y. By computing the Green's function in this geometry, it becomes evident that the periodicity leads to density modulations confined to a region next to the wall, of typical scale L_y. For simplicity, we present the derivation in two dimensions. Note that the main difference with the derivation of the main text is the different Green's function that needs to be used on the cylindrical shell. As we show, the derivation also allows us to obtain the finite-size corrections to the density-density correlation function used in the main text. This is important when comparing our theory to numerical results obtained in finite systems.

We first consider the case of an isolated deformation localized at some position y'. To obtain the correct Green's function, we note that Eq. (10) possesses conformal invariance [61] which allows to employ a conformal mapping. Consider first the Neumann-Green's function given by Eq (12), which corresponds to a Poisson equation with a point source located at the origin in the half-plane (u, v), $u > 0$ and $-\infty < v < \infty$:

$$G_N(u, v) = -\frac{1}{2\pi} \ln(u^2 + v^2). \tag{C1}$$

Next, place the periodic boundary conditions of our cylindrical domain to be at $(y - y') = \pm\frac{L_y}{2}$, such that they are equally distant from the source. The mapping between the two domains is a textbook problem on conformal mappings. Once complexified,[3] it is obtained by a Schwartz-Christoffel transformation [62] as illustrated in Fig. 10, which reads

$$u(x, y; y') = \sinh\left(\frac{\pi x}{L_y}\right) \cos\left(\frac{\pi (y - y')}{L_y}\right),$$
$$v(x, y; y') = \cosh\left(\frac{\pi x}{L_y}\right) \sin\left(\frac{\pi (y - y')}{L_y}\right). \tag{C2}$$

Let us briefly comment on why this mapping ensures the correct boundary conditions in the (x, y) cylindrical domain. The points $(u = 0, -1 < v < 1)$ are mapped onto the boundary $(x = 0, y)$. The Neumann boundary conditions in the (u, v) plane then ensures Neumann boundary conditions along the $(x = 0, y)$ segment. Then the lines $(u = 0, v > 1)$ and $(u = 0, v < -1)$ are mapped onto $(x, y = y' + \frac{L_y}{2})$ and $(x, y = y' - \frac{L_y}{2})$, respectively. Since conformal mapping preserve angles, the Neumann boundary conditions along $(u = 0, |v| > 1)$ ensure that the derivatives of the mapped Green's function along

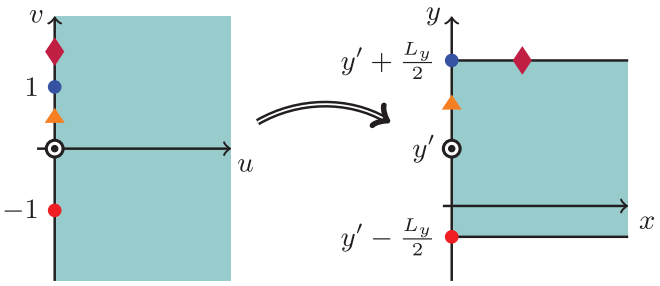

FIG. 10. To compute the Green's function in Eq. (C4), we start from that of a point source close to an infinite wall, given in Eq. (12). The domain is then transformed using a combination of conformal mapping techniques and properties of the Green's function into the domain shown in the right, where periodic boundary conditions are used along the $\hat{\mathbf{y}}$ direction.

$\hat{\mathbf{y}}$ vanish at $(x, y' \pm \frac{L_y}{2})$. Finally, the symmetry of the Green's function in the (u, v) plane with respect to $v \to -v$ at $u = 0$ ensures the periodicity of the mapped Green's function.

On the cylindrical shell, the Green's function of a point source localized at $(0, y')$ is thus

$$G(x, y; 0, y') = -\frac{1}{2\pi} \ln\left[u^2(x, y; y') + v^2(x, y; y')\right] \tag{C3}$$
$$= -\frac{1}{2\pi} \ln\left[\sinh^2\left(\frac{\pi x}{L_y}\right) \cos^2\left(\frac{\pi (y - y')}{L_y}\right) + \cosh^2\left(\frac{\pi x}{L_y}\right) \sin^2\left(\frac{\pi (y - y')}{L_y}\right)\right]. \tag{C4}$$

Finally, using the derivation of the main text, one then finds that a localized deformation on the wall around $(x, y) = (0, 0)$ leads to a density modulation that is given in the far field by

$$\rho(\mathbf{r}) \underset{x \gg a, \ell_p}{\simeq} \rho_b + \frac{\mu p}{\mathcal{D}_{\text{eff}} L_y} \frac{\sin\left(\frac{2\pi y}{L_y}\right)}{\cosh\left(\frac{2\pi x}{L_y}\right) - \cos\left(\frac{2\pi y}{L_y}\right)}, \tag{C5}$$

with

$$p = -\int_0^\infty dx' \int_0^{L_y} dy' \, \rho(\mathbf{r}') \partial'_y U. \tag{C6}$$

We study this result in two limits. First, we note that, far from the wall, for $x \gg L_y$, the density profile decays exponentially as $\exp(-2\pi x/L_y)$. The long-range decay observed next to an infinite, aperiodic wall is thus screened due to the periodic boundary conditions and decays exponentially on a scale set by the wall's periodicity.

Second, the exact expression for the Green's function obtained here allows us to understand how to compare the simulation results, obtained with a periodic disordered boundary condition along the $\hat{\mathbf{y}}$ direction, with the two-point correlation function computed in the main text (25) for a semi-infinite system. To do so, we calculate the connected two-point correlation function of the density field and analyze it in the $x \ll L_y$ limit. In the steady state, the far-field behavior of the two-dimensional density profile generated by

[3]The complexified domains are also compactified, adding a "point at infinity" [63].

a disordered wall reads

$$\rho(x,y)\simeq\rho_b+\frac{\mu}{\mathcal{D}_{\rm eff}L_y}\int_{-\frac{L_y}{2}}^{\frac{L_y}{2}}dy'\,\frac{\sin\left(\frac{2\pi(y-y')}{L_y}\right)f(y')}{\cosh\left(\frac{2\pi x}{L_y}\right)-\cos\left(\frac{2\pi(y-y')}{L_y}\right)}.$$

Here $f(y)$ is the force-monopole density, satisfying $\overline{f(y)}=0$ and $\overline{f(y)f(y')}=2p^2\sigma^2\delta(y-y')$, as in Eq. (22). With this, the disorder-averaged connected pair correlation function can be computed. For a periodicity L_y much larger than the separation between the points or their distances from the wall x, x', $\Delta y \ll L_y$, one finds

$$\overline{\rho(x,y)\rho(x',y')}_c\simeq\frac{2}{\pi}\left(\frac{\mu p\sigma}{\mathcal{D}_{\rm eff}}\right)^2\left[\frac{(x+x')}{(x+x')^2+(y-y')^2}-\frac{\pi}{L_y}+O\left(1/L_y^2\right)\right]. \tag{C7}$$

Note that to leading order in large L_y, this result coincides with the correlation induced by an infinite wall (25), showing a long-range decay of correlations.

Finally, the fact that the results obtained in the semi-infinite domain and using periodic boundary conditions agree up to a constant that decays as $1/L_y$ is a standard property of connected correlation functions. Integrating the left-hand side of Eq. (C7) along $\hat{\mathbf{y}}$ or $\hat{\mathbf{y}}'$ has to vanish by definition of the connected correlation function. The Lorentzian being strictly positive, a constant has to be subtracted from the semi-infinite domain solution. In the geometry considered here, we could use our exact result for the periodic Green's function to predict this constant exactly. In the other geometries considered in the article, and in the presence of interactions, we use this offset as a fitting parameter.

APPENDIX D: TWO PARALLEL WALLS

In this Appendix, we consider the density modulation induced by two parallel disordered walls. The disorder on each wall acts as random forcing independent of the disorder on the other wall. Its effect is modeled as a disordered force-monopole density, which satisfies

$$\begin{aligned}\overline{f_i^\alpha(\mathbf{r}_\parallel)}&=0,\\ \overline{f_i^\alpha(\mathbf{r}_\parallel)f_j^\beta(\mathbf{r}'_\parallel)}&=2p^2\delta_{ij}^\parallel\sigma^2\delta^{\alpha\beta}\delta^{(d-1)}(\mathbf{r}_\parallel-\mathbf{r}'_\parallel),\end{aligned} \tag{D1}$$

with the indices α,β denoting either the left or the right wall. In $d=2$, the exact form of the connected, two-point correlation function can be obtained by using a conformal mapping on the one-wall solution. Here we work in arbitrary dimension and follow the simpler approach of evaluating the correlation function to leading order in the separation between the walls, L_x.

In this limit, we can simply sum independently the contributions of the two walls, each computed with the Green's function of the semi-infinite domain, which leads to a density profile

$$\rho(x,\mathbf{r}_\parallel)\simeq\rho_b+\frac{\mu}{\mathcal{D}_{\rm eff}S_d}\int d^{d-1}\mathbf{r}_\parallel\left[\frac{(\mathbf{r}_\parallel-\mathbf{r}'_\parallel)\cdot\mathbf{f}^L(\mathbf{r}'_\parallel)}{[x^2+|\mathbf{r}_\parallel-\mathbf{r}'_\parallel|^2]^{\frac{d}{2}}}+\frac{(\mathbf{r}_\parallel-\mathbf{r}'_\parallel)\cdot\mathbf{f}^R(\mathbf{r}'_\parallel)}{[(L_x-x)^2+|\mathbf{r}_\parallel-\mathbf{r}'_\parallel|^2]^{\frac{d}{2}}}\right].$$

With this, it is straightforward to see that the connected, two-point correlation function is given by

$$\overline{\rho(x,\mathbf{r}_\parallel)\rho(x',\mathbf{r}'_\parallel)}_c\approx\frac{1}{S_d}\left(\frac{\mu p\sigma}{\mathcal{D}_{\rm eff}}\right)^2\left[\frac{(x+x')}{[(x+x')^2+|\mathbf{r}_\parallel-\mathbf{r}'_\parallel|^2]^{\frac{d}{2}}}+\frac{\{2L_x-(x+x')\}}{[2L_x-(x+x')]^2+|\mathbf{r}_\parallel-\mathbf{r}'_\parallel|^2]^{\frac{d}{2}}}\right]. \tag{D2}$$

Figure 6 compares this result with numerical measurements of the correlation function in two dimensions. Note that, since the numerics use periodic boundary conditions in the $\hat{\mathbf{y}}$ direction, the expression is expected to fit the data only for $|y-y'|\lesssim L_y$. To account for the finite size of the simulation box, following the results of Appendix C, we include a constant offset when we fit our numerical data to Eq. (D2).

APPENDIX E: STRUCTURE FACTOR OF THE LINEAR FIELD THEORY

Here we detail the calculation of the structure factor of our linear field theory. We start by writing the equation for the density modulation $\phi(\mathbf{r},t)$ using Eqs. (31) and (32). Performing a Fourier transform gives

$$\partial_t\phi(\mathbf{q},t)=-q^2g[\phi]-i\mathbf{q}\cdot[\mathbf{f}(\mathbf{q})+\sqrt{2D}\boldsymbol{\eta}(\mathbf{q},t)], \tag{E1}$$

where $g[\phi]=u\phi+Kq^2\phi$ is the Fourier transform of the chemical potential. The statistics of $\mathbf{f}(\mathbf{q})$ and $\boldsymbol{\eta}(\mathbf{q},t)$ are obtained using Eqs. (34) and (35) to give

$$\begin{aligned}\overline{f_i(q_x,\mathbf{q}_\parallel)}&=0,\\ \overline{f_i(q_x,\mathbf{q}_\parallel)f_j(q'_x,\mathbf{q}'_\parallel)}&=2s^2\delta_{ij}^\parallel(2\pi)^{d-1}\delta^{(d-1)}(\mathbf{q}_\parallel+\mathbf{q}_\parallel),\\ \langle\eta_i(\mathbf{q},t)\rangle&=0,\\ \langle\eta_i(\mathbf{q},t)\eta_j(\mathbf{q}',t')\rangle&=\delta_{ij}(2\pi)^d\delta^d(\mathbf{q}+\mathbf{q}')\delta(t-t').\end{aligned}$$

Here we decompose the wave vector as $\mathbf{q}=(q_x,\mathbf{q}_\parallel)$ where q_x is its x-component and $\mathbf{q}_\parallel$ corresponds to the components parallel to the wall.

The structure factor can then be computed directly by solving the linear inhomogeneous differential equation for $\phi(\mathbf{q},t)$ and evaluating $\overline{\langle\phi(\mathbf{q})\phi(\mathbf{q}')\rangle}$, leading to Eq. (37). The large-scale asymptotic expression of the structure factor is obtained

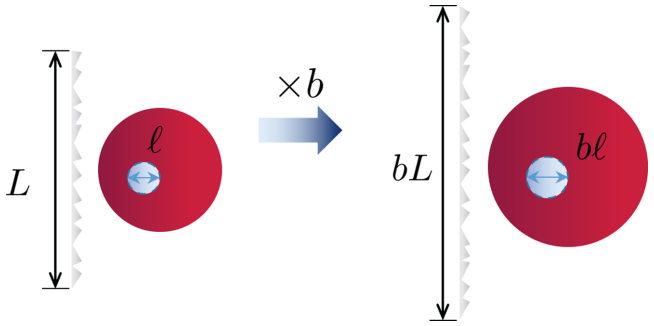

FIG. 11. The scaling argument presented in Fig. 9 for the wetting layer can be adapted to the case of a liquid droplet. Upon scaling the system size by a factor of b, we compare the scaling of the bulk and surface energies, whose competition determines if the droplet is macroscopically stable.

by taking the limit of small q. Performing an inverse Fourier transform on Eq. (38) then shows that the structure factor is consistent with the two-point correlation function predicted by the multipole expansion of Eq. (25).

APPENDIX F: THE IMRY-MA ARGUMENT FOR A DROPLET CONFIGURATION

Here we present an alternative version of the Imry-Ma argument presented in Sec. V. In contrast to the case discussed in the main text, we do not assume that the phase-separated state wets the wall. Instead, we consider a liquid bubble in the bulk of the system, surrounded by a gaseous phase, following the seminal work of Ref. [48]. As we show, both approaches lead to similar conclusions.

We consider the droplet of linear size ℓ shown in Fig. 11. The surface contribution to the free-energy scales as $E_\gamma = \gamma \ell^{d-1}$. To check the stability of this configuration, this should be compared to the bulk energy contribution of the effective potential induced by the boundary disorder $E_U = \int_{\ell^d} d^d\mathbf{r}\, \rho_0 U(\mathbf{r})$, where the integral goes over the volume of the droplet, which scales as ℓ^d. We now compare the scaling behaviors of E_γ and $|E_U|$ under an increase of the system size by a factor of b, $\mathbf{r} \to b\mathbf{r}$. The surface energy scales as $E_\gamma \to b^{d-1} E_\gamma$, while the scaling of the $|E_U|$ can be estimated from

$$\begin{aligned}\overline{E_U^2} &\to \rho_0^2 \int_{(b\ell)^d} d^d\mathbf{r} \int_{(b\ell)^d} d^d\mathbf{r}'\, \overline{U(\mathbf{r})U(\mathbf{r}')} \\ &= b^{d+1} \int_{\ell^d} d^d\mathbf{r} \int_{\ell^d} d^d\mathbf{r}'\, \frac{\left(s^2\rho_0^2/S_d\right)(x+x')}{[(x+x')^2 + |\Delta\mathbf{r}_\parallel|^2]^{d/2}},\end{aligned}$$

where the change of variables $\mathbf{r} \to b\mathbf{r}$ was carried out in the second line. The droplet bulk energy is thus rescaled as $|E_U| \to b^{\frac{d+1}{2}} |E_U|$.

Comparing the scaling of E_γ and E_U shows that the surface energy dominates the bulk contribution when the dimension satisfies

$$\frac{d+1}{2} < d-1 \quad \text{i.e.,} \quad 3 < d. \tag{F1}$$

The analysis, as expected, agrees with the Imry-Ma argument of the main text, showing that the phase-separated state is unstable in dimensions smaller than $d_c = 3$.

[1] T. Vicsek and A. Zafeiris, Collective motion, Phys. Rep. **517**, 71 (2012).

[2] P. Romanczuk, M. Bär, W. Ebeling, B. Lindner, and L. Schimansky-Geier, Active Brownian particles, Eur. Phys. J.: Spec. Top. **202**, 1 (2012).

[3] M. Marchetti, J. Joanny, S. Ramaswamy, T. Liverpool, J. Prost, M. Rao, and T. Aditi Simha, Hydrodynamics of soft active matter, Rev. Mod. Phys. **85**, 1143 (2013).

[4] M. E. Cates and J. Tailleur, Motility-induced phase separation, Annu. Rev. Condens. Matter Phys. **6**, 219 (2015).

[5] C. Bechinger, R. Di Leonardo, H. Löwen, C. Reichhardt, G. Volpe, and G. Volpe, Active particles in complex and crowded environments, Rev. Mod. Phys. **88**, 045006 (2016).

[6] F. S. Gnesotto, F. Mura, J. Gladrow, and C. P. Broedersz, Broken detailed balance and non-equilibrium dynamics in living systems: A review, Rep. Prog. Phys. **81**, 066601 (2018).

[7] J. O'Byrne, Y. Kafri, J. Tailleur, and F. van Wijland, Time-irreversibility in active matter: From micro to macro, Nat. Rev. Phys. **4**, 167 (2022).

[8] J. Toner and Y. Tu, Flocks, herds, and schools: A quantitative theory of flocking, Phys. Rev. E **58**, 4828 (1998).

[9] J. Tailleur and M. E. Cates, Statistical Mechanics of Interacting Run-and-Tumble Bacteria, Phys. Rev. Lett. **100**, 218103 (2008).

[10] A. Thompson, J. Tailleur, M. Cates, and R. Blythe, Lattice models of nonequilibrium bacterial dynamics, J. Stat. Mech.: Theory Exp. (2011) P02029.

[11] Y. Fily and M. C. Marchetti, Athermal Phase Separation of Self-Propelled Particles with no Alignment, Phys. Rev. Lett. **108**, 235702 (2012).

[12] H. H. Wensink, J. Dunkel, S. Heidenreich, K. Drescher, R. E. Goldstein, H. Löwen, and J. M. Yeomans, Meso-scale turbulence in living fluids, Proc. Natl. Acad. Sci. USA **109**, 14308 (2012).

[13] J. Palacci, S. Sacanna, A. P. Steinberg, D. J. Pine, and P. M. Chaikin, Living crystals of light-activated colloidal surfers, Science **339**, 936 (2013).

[14] I. Buttinoni, J. Bialké, F. Kümmel, H. Löwen, C. Bechinger, and T. Speck, Dynamical Clustering and Phase Separation in Suspensions of Self-Propelled Colloidal Particles, Phys. Rev. Lett. **110**, 238301 (2013).

[15] M. E. Cates and J. Tailleur, When are active Brownian particles and run-and-tumble particles equivalent? Consequences for motility-induced phase separation, Europhys. Lett. **101**, 20010 (2013).

[16] J. Stenhammar, A. Tiribocchi, R. J. Allen, D. Marenduzzo, and M. E. Cates, Continuum Theory of Phase Separation Kinetics for Active Brownian Particles, Phys. Rev. Lett. **111**, 145702 (2013).

[17] G. S. Redner, M. F. Hagan, and A. Baskaran, Structure and Dynamics of a Phase-Separating Active Colloidal Fluid, Phys. Rev. Lett. **110**, 055701 (2013).

[18] A. P. Solon, M. E. Cates, and J. Tailleur, Active Brownian particles and run-and-tumble particles: A comparative study, Eur. Phys. J.: Spec. Top. **224**, 1231 (2015).

[19] G. S. Redner, C. G. Wagner, A. Baskaran, and M. F. Hagan, Classical Nucleation Theory Description of Active Colloid Assembly, Phys. Rev. Lett. **117**, 148002 (2016).

[20] S. Paliwal, J. Rodenburg, R. van Roij, and M. Dijkstra, Chemical potential in active systems: Predicting phase equilibrium from bulk equations of state? New J. Phys. **20**, 015003 (2018).

[21] A. P. Solon, J. Stenhammar, M. E. Cates, Y. Kafri, and J. Tailleur, Generalized thermodynamics of phase equilibria in scalar active matter, Phys. Rev. E **97**, 020602(R) (2018).

[22] E. Tjhung, C. Nardini, and M. E. Cates, Cluster Phases and Bubbly Phase Separation in Active Fluids: Reversal of the Ostwald Process, Phys. Rev. X **8**, 031080 (2018).

[23] M. Kourbane-Houssene, C. Erignoux, T. Bodineau, and J. Tailleur, Exact Hydrodynamic Description of Active Lattice Gases, Phys. Rev. Lett. **120**, 268003 (2018).

[24] S. Whitelam, K. Klymko, and D. Mandal, Phase separation and large deviations of lattice active matter, J. Chem. Phys. **148**, 154902 (2018).

[25] D. Geyer, D. Martin, J. Tailleur, and D. Bartolo, Freezing a Flock: Motility-Induced Phase Separation in Polar Active Liquids, Phys. Rev. X **9**, 031043 (2019).
[26] H. Chaté, Dry aligning dilute active matter, Annu. Rev. Condens. Matter Phys. **11**, 189 (2020).
[27] A. Kudrolli, G. Lumay, D. Volfson, and L. S. Tsimring, Swarming and Swirling in Self-Propelled Polar Granular Rods, Phys. Rev. Lett. **100**, 058001 (2008).
[28] J. Deseigne, O. Dauchot, and H. Chate, Collective Motion of Vibrated Polar Disks, Phys. Rev. Lett. **105**, 098001 (2010).
[29] F. G. Woodhouse and R. E. Goldstein, Spontaneous Circulation of Confined Active Suspensions, Phys. Rev. Lett. **109**, 168105 (2012).
[30] H. Wioland, F. G. Woodhouse, J. Dunkel, J. O. Kessler, and R. E. Goldstein, Confinement Stabilizes a Bacterial Suspension into a Spiral Vortex, Phys. Rev. Lett. **110**, 268102 (2013).
[31] A. Bricard, J.-B. Caussin, D. Das, C. Savoie, V. Chikkadi, K. Shitara, O. Chepizhko, F. Peruani, D. Saintillan, and D. Bartolo, Emergent vortices in populations of colloidal rollers, Nat. Commun. **6**, 1 (2015).
[32] H. Wioland, F. G. Woodhouse, J. Dunkel, and R. E. Goldstein, Ferromagnetic and antiferromagnetic order in bacterial vortex lattices, Nat. Phys. **12**, 341 (2016).
[33] A. Souslov, B. C. Van Zuiden, D. Bartolo, and V. Vitelli, Topological sound in active-liquid metamaterials, Nat. Phys. **13**, 1091 (2017).
[34] A. Sokolov, M. Apodaca, B. Grzybowski, and I. Aranson, Swimming bacteria power microscopic gears, Proc. Natl. Acad. Sci. USA **107**, 969 (2010).
[35] R. Di Leonardo, L. Angelani, D. Della Arciprete, G. Ruocco, V. Iebba, S. Schippa, M. Conte, F. Mecarini, F. De Angelis, and E. Di Fabrizio, Bacterial ratchet motors, Proc. Natl. Acad. Sci. USA **107**, 9541 (2010).
[36] N. Nikola, A. P. Solon, Y. Kafri, M. Kardar, J. Tailleur, and R. Voituriez, Active Particles with Soft and Curved Walls: Equation of State, Ratchets, and Instabilities, Phys. Rev. Lett. **117**, 098001 (2016).
[37] H. Chaté and B. Mahault, Dry, aligning, dilute, active matter: A synthetic and self-contained overview, arXiv:1906.05542 (2019).
[38] J. L. Lebowitz, Statistical mechanics: A selective review of two central issues, Rev. Mod. Phys. **71**, S346 (1999).
[39] J. Elgeti and G. Gompper, Wall accumulation of self-propelled spheres, Europhys. Lett. **101**, 48003 (2013).
[40] J. Elgeti and G. Gompper, Self-propelled rods near surfaces, Europhys. Lett. **85**, 38002 (2009).
[41] J. Tailleur and M. Cates, Sedimentation, trapping, and rectification of dilute bacteria, Europhys. Lett. **86**, 60002 (2009).
[42] J. D. Jackson, *Classical Electrodynamics*, 3rd ed. (Wiley, New York, 1999).
[43] Y. Baek, A. P. Solon, X. Xu, N. Nikola, and Y. Kafri, Generic Long-Range Interactions between Passive Bodies in an Active Fluid, Phys. Rev. Lett. **120**, 058002 (2018).
[44] S. C. Takatori, W. Yan, and J. F. Brady, Swim Pressure: Stress Generation in Active Matter, Phys. Rev. Lett. **113**, 028103 (2014).
[45] X. Yang, M. Manning, and M. Marchetti, Aggregation and segregation of confined active particles, Soft Matter **10**, 6477 (2014).
[46] A. Solon, Y. Fily, A. Baskaran, M. Cates, Y. Kafri, M. Kardar, and J. Tailleur, Pressure is not a state function for generic active fluids, Nat. Phys. **11**, 673 (2015).
[47] Y. Fily, Y. Kafri, A. P. Solon, J. Tailleur, and A. Turner, Mechanical pressure and momentum conservation in dry active matter, J. Phys. A: Math. Theor. **51**, 044003 (2017).
[48] Y. Imry and S.-k. Ma, Random-Field Instability of the Ordered State of Continuous Symmetry, Phys. Rev. Lett. **35**, 1399 (1975).
[49] A. Aharony, Y. Imry, and S.-k. Ma, Lowering of Dimensionality in Phase Transitions with Random Fields, Phys. Rev. Lett. **37**, 1364 (1976).
[50] A. N. Berker, Ordering under random fields: Renormalization-group arguments, Phys. Rev. B **29**, 5243 (1984).
[51] M. Kardar, Domain walls subject to quenched impurities, J. Appl. Phys. **61**, 3601 (1987).
[52] See Supplemental Material at http://link.aps.org/supplemental/10.1103/PhysRevE.105.044603 for a movie showing a MIPS bubble dissolving due to boundary disorder, switched on at $t = 0$.
[53] D. E. Feldman and V. M. Vinokur, Destruction of Bulk Ordering by Surface Randomness, Phys. Rev. Lett. **89**, 227204 (2002).
[54] G. Szamel, Self-propelled particle in an external potential: Existence of an effective temperature, Phys. Rev. E **90**, 012111 (2014).
[55] D. Martin, J. O'Byrne, M. E. Cates, É. Fodor, C. Nardini, J. Tailleur, and F. van Wijland, Statistical mechanics of active Ornstein-Uhlenbeck particles, Phys. Rev. E **103**, 032607 (2021).
[56] P. Galajda, J. Keymer, P. Chaikin, and R. Austin, A wall of funnels concentrates swimming bacteria, J. Bacteriol. **189**, 8704 (2007).
[57] R. Soto and R. Golestanian, Run-and-tumble dynamics in a crowded environment: Persistent exclusion process for swimmers, Phys. Rev. E **89**, 012706 (2014).
[58] D. S. Dean, Langevin equation for the density of a system of interacting Langevin processes, J. Phys. A: Math. Gen. **29**, L613 (1996).
[59] A. P. Solon, J. Stenhammar, R. Wittkowski, M. Kardar, Y. Kafri, M. E. Cates, and J. Tailleur, Pressure and Phase Equilibria in Interacting Active Brownian Spheres, Phys. Rev. Lett. **114**, 198301 (2015).
[60] O. Granek, Y. Baek, Y. Kafri, and A. P. Solon, Bodies in an interacting active fluid: Far-field influence of a single body and interaction between two bodies, J. Stat. Mech.: Theory Exp. (2020) 063211.
[61] J. Kevorkian, *Partial Differential Equations: Analytical Solution Techniques*, 2nd ed., Texts in Applied Mathematics (Springer, 2000).
[62] M. J. Ablowitz, A. S. Fokas, and A. S. Fokas, *Complex Variables: Introduction and Applications* (Cambridge University Press, 2003).
[63] D. Sarason, *Notes on Complex Function Theory* (H. Helson, 1994).